# Spatio-temporal evolution of intraplate strike-slip faulting: The Neogene–Quaternary Kuh-e-Faghan Fault, central Iran

**Gabriele Calzolari[1], Federico Rossetti[1,†], Marta Della Seta[2], Reza Nozaem[3], Valerio Olivetti[4], Maria Laura Balestrieri[5], Domenico Cosentino[1], Claudio Faccenna[1], Finlay M. Stuart[6], and Gianluca Vignaroli[1]**

[1]*Dipartimento di Scienze, Università Roma Tre, Largo S.L. Murialdo 1, 00146 Roma, Italy*

[2]*Dipartimento di Scienze della Terra, "Sapienza" Università di Roma, Piazzale Aldo Moro 5, 00185 Rome, Italy*

[3]*Department of Geology, Imam Khomeini International University, 34149-16818 Qazvin, Iran*

[4]*Aix-Marseille Université, Centre National de la Recherche Scientifique, Institut de Recherche pour le Développement, CEREGE UM34, 13545 Aix en Provence, France*

[5]*Consiglio Nazionale delle Ricerche, Istituto di Geoscienze e Georisorse, Via G. La Pira 4, 50121 Firenze, Italy*

[6]*Scottish Universities Environmental Research Centre, Scottish Enterprise Technology Park, East Kilbride G75 0QF, UK*

## ABSTRACT

**Central Iran provides an ideal region in which to study the long-term morphotectonic response to the nucleation and propagation of intraplate faulting. In this study, a multidisciplinary approach that integrates structural and stratigraphic field investigations with apatite (U + Th)/He (AHe) thermochronometry is used to reconstruct the spatio-temporal evolution of the Kuh-e-Faghan Fault in northeastern central Iran. The Kuh-e-Faghan Fault is a narrow, ~80-km-long, deformation zone that consists of three main broadly left-stepping, E-W–trending, dextral fault strands that cut through the Mesozoic–Paleozoic substratum and the Neogene–Quaternary sedimentary cover. The AHe thermochronometry results indicate that the intrafault blocks along the Kuh-e-Faghan Fault experienced two major episodes of fault-related exhumation at ca. 18 Ma and ca. 4 Ma. The ca. 18 Ma faulting/exhumation episode is chiefly recorded by the structure and depositional architecture of the Neogene deposits along the Kuh-e-Faghan Fault. A source-to-sink scenario can be reconstructed for this time frame, where topographic growth caused the synchronous erosion/exhumation of the pre-Neogene units and deposition of the eroded material in the surrounding fault-bounded continental depocenters. Successively, the Kuh-e-Faghan Fault gradually entered a period of relative tectonic quiescence and, probably, of regional subsidence, during which a thick pile of fine-grained onlapping sediments was deposited. This may have caused resetting of the He ages of apatite in the pre-Neogene and the basal Neogene successions. The ca. 4 Ma faulting episode caused the final exhumation of the fault system, resulting in the current fault zone and topography. The two fault-related exhumation episodes fit with regional early Miocene collision-enhanced uplift/exhumation, and the late Miocene–early Pliocene widespread tectonic reorganization of the Iranian Plateau. The reconstructed long-term, spatially and temporally punctuated fault system evolution in intraplate central Iran during Neogene–Quaternary times may reflect states of far-field stress changes at the collisional boundaries.**

## INTRODUCTION

As demonstrated by regional and global stress field maps, in-plane stresses can be transferred from the plate margins across large distances through continental and oceanic lithosphere (e.g., Zoback, 1992; Sandiford et al., 2004; Cloetingh et al., 2005; Heidbach et al., 2008). This is best illustrated in regions affected by continental collision, where seismicity extends deep into the continental plate interiors, thus defining broad and diffuse zones of deformation (e.g., central Iran, Turkey, and Tibetan Plateau; Hatzfeld and Molnar, 2010). In such settings, the transmission of compressive stresses and distribution of deformation in intraplate settings are dominantly a function of the spatial and temporal changes in plate-boundary dynamics (Raimondo et al., 2014) and, in particular, of the degree of tectonic coupling at the collisional interface (Ellis, 1996; Ziegler et al., 1998).

Studies on intraplate deformation demonstrate that strike-slip faulting is the primary process by which such horizontal movements are accommodated and stresses are transferred further away from the collision front (e.g., Molnar and Tapponnier, 1975; Bayasgalan et al., 1999; Calais et al., 2003; Storti et al., 2003; Vernant et al., 2004; Simons et al., 2007; Reece et al., 2013; Allen et al., 2011; Walpersdorf et al., 2014). Strike-slip–dominated continental deformation zones typically consist of interlinked systems of fault- and shear zone–bounded blocks that partition strain to form complex regions of displacement, internal distortion, and rigid block rotations at various scales (e.g., Ron et al., 1984; Christie-Blick and Biddle, 1985; Silvester, 1988; Woodcock and Schubert, 1994; Storti et al., 2003; Cunningham and Mann, 2007). This is mostly due to the structural inheritance of continental crust and lithosphere acquired through the continuous incorporation of plate-margin structures by continental collision and accretion processes that operate for geologically long periods of time (e.g., Molnar, 1988; Ziegler et al., 1998; Matenco et al., 2007; Dyksterhuis and Müller, 2008; Aitken et al., 2013; Raimondo et al., 2014). Such structures constitute major subvertical weak zones of mechanical anisotropy and strain softening, which, once incorporated into the plate interiors, may be readily reactivated as strike-slip–dominated deformation zones at various spatial and temporal scales (e.g., Tapponnier and Molnar, 1977; Sutton and Watson, 1986; Salvini et al., 1997; Tavarnelli, 1998; Tavarnelli and Holdsworth, 1999; Tavarnelli and Pasqui, 2000; Holdsworth et al., 2001; Webb and Johnson, 2006; Allen et al., 2011; Rossetti et al., 2003; Morley, 2007; Di Vincenzo et al., 2013; Avouac et al., 2014). The longevity

†federico rossetti@uniroma3.it

of intraplate strike-slip fault systems and their linkage to plate-boundary dynamics make them excellent strain markers of the intraplate deformation response to continental collision. An understanding of the spatial and temporal distribution of crustal deformation accommodated along strike-slip faults is therefore central to unravel the regimes and modes through which continental tectonics operate.

The cause of crustal strain, topographic growth, and exhumation along strike-slip faults is a complex feedback between near-field (<20 km) boundary conditions and far-field plate-tectonic driving mechanisms (Spotila et al., 2001; Buscher and Spotila, 2007). Moreover, several processes and conditions have been invoked to explain topographic growth and focused exhumation along strike-slip systems, and these processes may play an important role in regional exhumation and topographic patterns: (1) the degree of obliquity of the plate motion vector with respect to the fault trace (e.g., Sanderson and Marchini, 1984; Fitzgerald et al., 1993, 1995; Spotila et al., 1998); (2) structural irregularities such as stepovers (Aydin and Nur, 1985; Hilley and Arrowsmith, 2008; Finzi et al., 2009; Carne and Little, 2012); (3) variations in master fault dip (Dair and Cooke, 2009); (4) enhanced erosion due to pervasive tectonically induced fracturing and associated volume increase (Braun, 1994; Schopfer and Steyrer, 2001; Le Guerroué and Cobbold, 2006; Molnar et al., 2007; Schrank and Cruden, 2010; Cox et al., 2012); and (5) climate forcings (Headley et al., 2013; Pavlis et al., 2014). Furthermore, the amount of exhumation along a strike-slip fault is not always simply correlated with the degree of transpression or with the composition of the juxtaposed rocks (Spotila et al., 2007).

This study describes the Neogene–Quaternary structural and stratigraphic evolution and exhumation history of the Kuh-e-Faghan Fault system, a major shear belt situated at the northern margin of the Lut block in central Iran (Fig. 1). The aim is to understand: (1) how intraplate tectonic deformation propagates and evolves in space and time; and (2) its impact on long-term, fault-controlled landscape evolution. Field studies are integrated with apatite (U + Th)/He (AHe) thermochronometry to link structures to the distribution of topographic relief and spatial variations in exhumation rate. We document E-W–oriented, dextral strike-slip tectonics associated with two distinct episodes of fault-related exhumation at ca. 18 Ma and ca. 4 Ma. A conceptual model of fault initiation and propagation is then proposed that has implications for the activation and kinematic evolution of the intraplate strike-slip fault systems in central Iran during Neogene–Quaternary times.

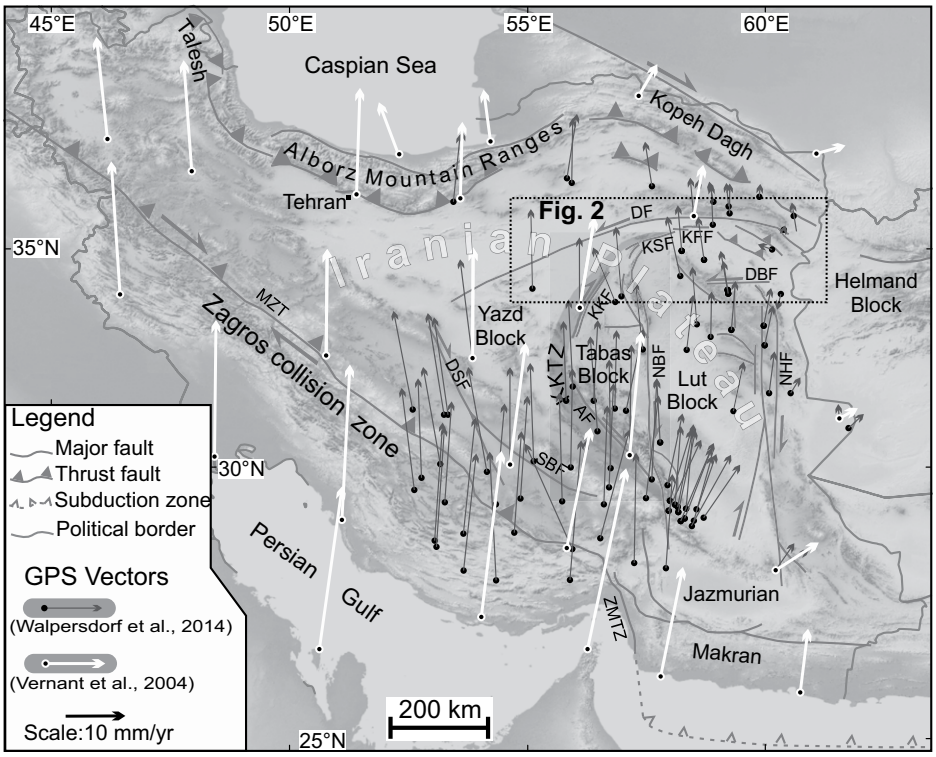


**Figure 1. Simplified tectonic map of Iran, showing the main collisional and intraplate strike-slip fault domains accommodating the Arabia-Eurasia convergence (modified after Berberian and King, 1981). The dashed rectangle indicates the study area. AF—Anar fault; DBF—Dasht-e-Bayaz fault; DF—Doruneh fault; DSF—Dehshir fault; KFF— Kuh-e-Faghan Fault; KKF—Kalmard-Kuhbanan fault; KKTZ—Kashmar-Kerman tectonic zone; KSF—Kuh-e-Sarhangi fault; MZT—Main Zagros thrust; NBF—Nayband fault; NHF—Nehbandan fault; SBF—Shahr-e-Babak fault; ZMTZ—Zagros-Makran transfer zone. The GPS velocities vectors in Iran relative to stable Eurasia are shown with different colors after Vernant et al. (2004) and Walpersdorf et al. (2014).**

## GEOLOGICAL BACKGROUND

The Arabia-Eurasia collision zone is one of the largest and most spectacular examples of continental convergent deformation on Earth (Hatzfeld and Molnar, 2010). Convergence may have initiated in the mid-Jurassic (e.g., Agard et al., 2011) and culminated with the Arabia-Eurasia continental collision through a polyphase tectonic history that involved the following phases: (1) Collision is estimated to have started at the Eocene-Oligocene boundary (e.g., Hessami et al., 2001; McQuarrie et al., 2003; Hafkenscheid et al., 2006; Robertson et al., 2006; Vincent et al., 2007; Allen and Armstrong, 2008; Homke et al., 2009, 2010; Mouthereau et al., 2012). (2) A regional increase in collision-related uplift, exhumation, and subsidence in adjacent basins began in the early Miocene, as documented by low-temperature thermochronometric (Axen et al., 2001; Guest et al., 2006; Verdel et al., 2007; Gavillot et al., 2010; Homke et al., 2010; Okay et al., 2010; Khadivi et al., 2012; Ballato et al., 2013; Madanipour et al., 2013), stratigraphic (e.g., Hessami et al., 2001; Guest et al., 2006; Mouthereau et al., 2007; Ballato et al., 2008; Morley et al., 2009; Khadivi et al., 2010; Ballato et al., 2011) and structural (e.g., Allen et al., 2004; Mouthereau et al., 2007) evidence. (3) A widespread tectonic reorganization during the late Miocene–early Pliocene is attested by enhanced exhumation in the Alborz and Talesh Mountains (Axen et al., 2001; Rezaeian et al., 2012; Madanipour et al., 2013) and fault kinematic changes in the Kopeh Dagh (Shabanian et al., 2009a, 2009b, 2010; Robert et al., 2014) and in the Zagros-Makran transfer zone (Regard et al., 2005), which are thought to have resulted in the current regional kinematic configuration (Allen et al., 2004). The evidence gathered in those studies principally comes from the orogenic belts situated at the edges of the Iranian Plateau (Fig. 1; Zagros Alborz, Kopeh Dagh, and Talesh). In contrast, little is known

about the deformation history of the intraplate domain of central Iran.

The Central East Iran microcontinent consists of an amalgamation of continental blocks bordered by topographically prominent mountain ranges, including the Kopeh Dagh, Alborz, and Talesh orogenic belts to the north, and the Zagros orogenic belt and Makran active subduction related complex to the northwest and south (Fig. 1). In particular, the Central East Iran microcontinent includes the Lut, Tabas, and Yazd microblocks (Aghanabati, 2004), which are bounded by linear mountain belts developed along major strike-slip fault zones that each have their distinct stratigraphy, deformation style, and pattern of recent seismicity (Berberian and King, 1981; Berberian, 2014).

The global positioning system (GPS) displacement vectors indicate a NNE motion of the Arabian plate relative to Eurasia of ~25 mm/yr (Sella et al., 2002; McClusky et al., 2003; Vernant et al., 2004; Reilinger et al., 2006; Walpersdorf et al., 2014). Such convergence is mostly absorbed in the orogenic terrains through contractional deformation (Zagros, Alborz, Kopeh Dagh, and Talesh in the north; Fig. 1). The Central East Iran microcontinent is moving northward at 6–13 mm/yr with respect to the stable Afghan crust at the eastern edge of the collision zone (Walpersdorf et al., 2014). Such differential motion is largely accommodated by the active strike-slip faults systems bounding the Central East Iran microcontinent, which are organized into N-S dextral (from west to east: the Deshir, Anar, Nayband-Gowk, and Nehbandan faults) and E-W sinistral (from north to south: Doruneh and Dasht-e Bayaz faults) shears (Fig. 1). Various studies have detailed present kinematics and total cumulative shear along the active strike-slip faults systems of central Iran, using geologic and geomorphic displaced markers identified from satellite imagery (Walker and Jackson, 2004; Allen et al., 2004, 2011; Meyer et al., 2006; Meyer and Le Dortz, 2007; Farbod et al., 2011). Taking into account the present-day slip rates (~2–10 mm/yr) along the major fault systems, the onset of strike-slip tectonics is inferred to date back to ca. 5 Ma (Allen et al., 2004). This shear pattern is commonly assumed to be accompanied by diffuse rigid block rotation and strain partitioning during ongoing Arabia-Eurasia convergence (Jackson and McKenzie, 1984; Walker et al., 2004; Walker and Jackson, 2004; Walker and Khatib, 2006; Fattahi et al., 2007; Allen et al., 2011; Farbod et al., 2011). Significant, post-Miocene counterclockwise rotation (25–35°), assumed to be accommodated along the major N-S–striking dextral fault systems, was documented in the Lut and Tabas blocks, whereas no significant rotation has been detected north of the Doruneh fault (Mattei et al., 2012). In particular, modeling the GPS data with a block rotation model suggests that the rotations have been going on at a similar rate (1 ± 0.4°/m.y.) over the last 12 m.y. (Walpersdorf et al., 2014). Nonetheless, evidence is provided to indicate that the Deshir and Anar faults (Fig. 1) are accommodating relative motion between nonrotating blocks, and strike-slip faulting is not confined to the Lut edges, but also occurs in central Iran, suggesting a nonrigid behavior of the Central East Iran microcontinent at least during the last 25 m.y. (Meyer et al., 2006; Meyer and LeDortz, 2007).

In a recent study, Nozaem et al. (2013) documented important post-Neogene to Quaternary dextral strike-slip tectonics along the Kuh-e-Sarhangi fault on the northwestern edge of the Lut block (Fig. 1), less than 40 km south of the subparallel, active sinistral Doruneh fault (Tchalenko et al., 1973; Fattahi et al., 2007; Farbod et al., 2011). This post-Neogene faulting is proposed to have occurred due to the tectonic reactivation of the northeastward extension of the late Neoproterozoic to early Paleozoic Kashmar-Kerman tectonic zone (Fig. 1; Ramezani and Tucker, 2003; Rossetti et al., 2015) in response to a kinematically induced stress field scenario (Nozaem et al., 2013). Similarly, Javadi et al. (2013) documented a polyphase kinematic history for the Doruneh fault, with a change from dextral to sinistral motion during late Miocene–early Pliocene times.

## KUH-E-FAGHAN FAULT ZONE

Our study focuses on a linear mountainous ridge (~80 km long and ~15 km wide; maximum elevation of ~1700 m), associated with the E-W–oriented Kuh-e-Faghan Fault (Figs. 1–3). This fault system forms the northern termination of the Kuh-e-Sarhangi fault system (Nozaem et al., 2013) and is located 25 km south of the Doruneh fault, continuing eastward for ~80 km (Fig. 2). The Kuh-e-Faghan Fault system and the surrounding areas are seismically active (Fig. 2), with maximum recorded

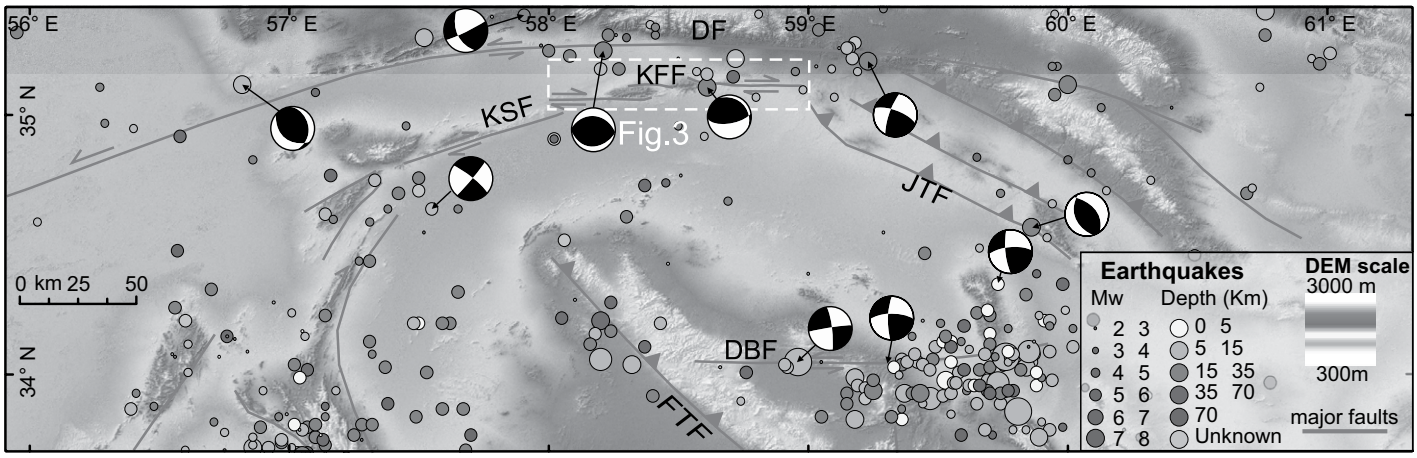


**Figure 2. Simplified tectonic map of northern central Iran, showing the historical and instrumental seismicity of the area. Focal mechanisms are taken from the Harvard catalog (http://www.globalcmt.org/CMTsearch.html). Epicenters are from the International Seismic Centre EHB Bulletin (International Seismic Centre, Thatcham, UK, 2009, (http://www.isc.ac.uk) and earthquake catalogue at Iranian Institute of Earthquake Engineering and Seismology (http://www.iiees.ac.ir). The dashed rectangle indicates the location of the study area and the extent of the map in Figure 3. DF—Doruneh fault; KSF—Kuh-e-Sarhangi fault; KFF—Kuh-e-Faghan Fault; JTF—Jangal Thrust Fault; DBF—Dasht-e-Bayaz fault.**

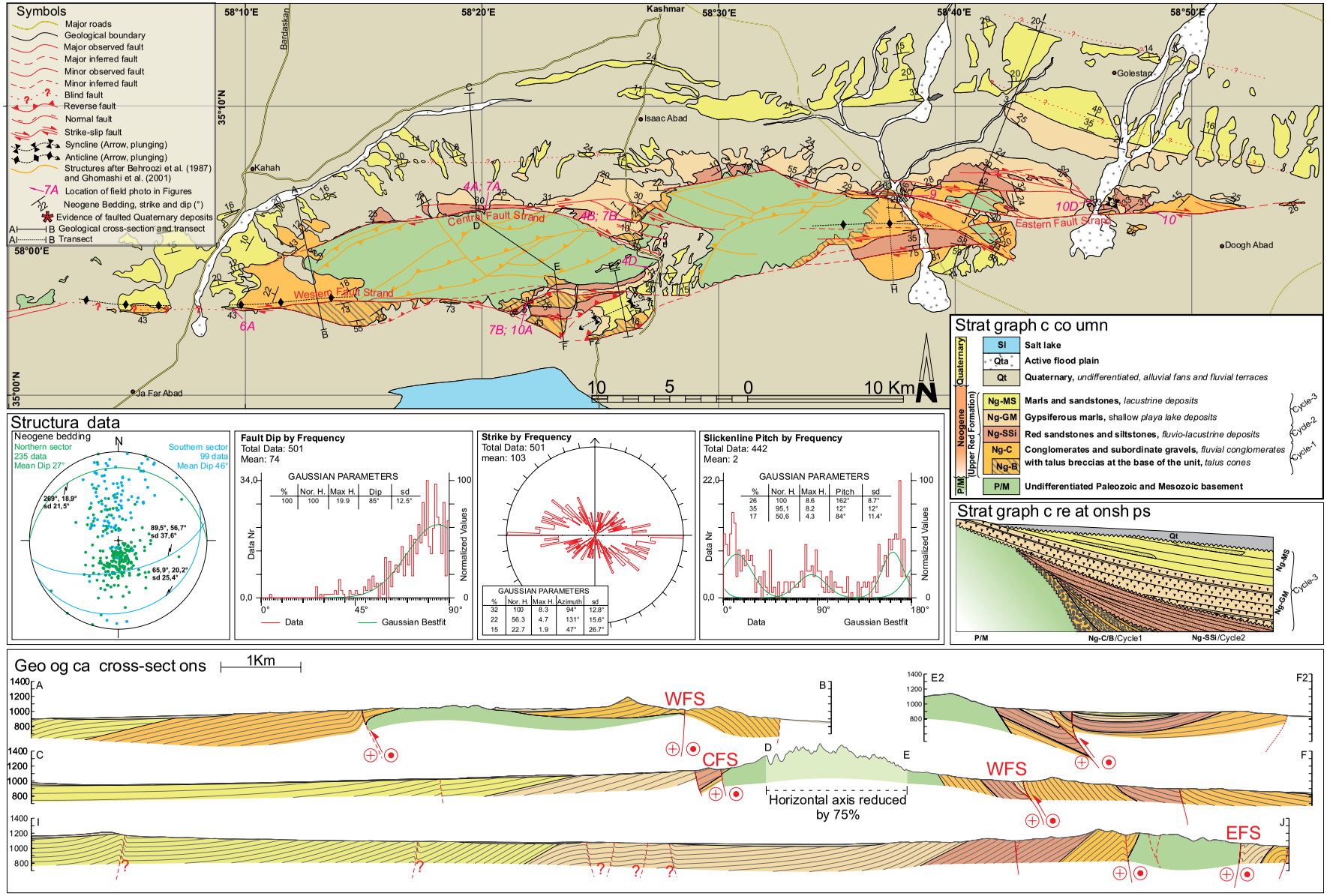


**Figure 3. Structural map of the study area and interpretative geological cross section (solid lines) across the structure of the Kuh-e-Faghan Fault. The inset shows the cumulative structural data set showing the bedding attitude (projected as pole to plane on a Schmidt net, lower-hemisphere projection) in the Neogene deposits and the cumulative polymodal Gaussian statistics (with errors quoted at 1σ [sd] level) as obtained from the collected fault population. Results are shown as rose diagram for strikes, and frequency distribution histograms for dip and slickenline pitch values (data processing through the software DAISY3; Salvini, 2004; http://host.uniroma3.it/progetti/fralab/). WFS—western fault strand; EFS—eastern fault strand; CFS—central fault strand.**

seismic magnitude between 4 and 5.5 and focal depths <35 km (Farbod et al., 2011).

The Kuh-e-Faghan Fault is an E-W–oriented brittle deformation zone that cuts pre-Neogene units (Paleozoic–Mesozoic successions, made of slightly or unmetamorphosed carbonates, and subordinate shales and sandstones; hereafter referred as basement units) and the unconformably overlying Neogene and Quaternary continental successions (Fig. 3; Eftekhar-Nezhad et al., 1976; Behroozi et al., 1987; Jalilian et al., 1992; Ghomashi et al., 2001). Fault kinematics along the Kuh-e-Faghan Fault are poorly described, with strike-slip (Eftekhar-Nezhad et al., 1976; Behroozi et al., 1987; Jalilian et al., 1992; Ghomashi et al., 2001) or reverse (Hassami et al., 2003; Javadi et al., 2013) kinematics having been proposed.

Paleogeographic and sedimentological studies (Berberian and King, 1981; Amini, 1997) refer the Neogene deposits alongside the Kuh-e-Faghan Fault to the Upper Red Formation of central Iran (Berberian, 1974). The Upper Red Formation is the oldest continental deposit unconformably lying above the marine, late Oligocene–middle Miocene Qom Formation (Berberian, 1974; Daneshian and Dana, 2007; Ballato et al., 2008; Hadavi et al., 2010). It consists of kilometer-thick alternating conglomerates, sandstones, siltstones, marls, and evaporites (Amini, 1997; Ballato et al., 2008; Morley et al., 2009; Ballato et al., 2011). Due to the lack of biostratigraphical markers or radiometrically datable units, the age and duration of the Upper Red Formation are not well constrained. Based on magnetostratigraphic study of the Eyvanekey section in the southern Alborz Mountains, Ballato et al. (2008) proposed a Burdigalian to Tortonian (17.5–7.5 Ma) age.

Quaternary successions unconformably cover the Upper Red Formation deposits and consist of alluvial fans and terraced alluvial plain deposits. Similar generations of alluvial fans, as well as regional arrangement of river terraces, have been recognized in the neighboring regions of eastern Iran and explained in terms of late Pleistocene and Holocene environmental changes (Walker and Fattahi, 2011). In particular, an infrared optically stimulated luminescence age of ≤10 ka (end of the Last Glacial Maximum) was obtained for the deposition of the Shesh-Taraz fan along the Doruneh fault (Fig. 1; Fattahi et al., 2007).

## NEOGENE STRATIGRAPHY

The Upper Red Formation of the study area is an ~4-km-thick, fining-upward succession of continental deposits, which include three main unconformity-bounded stratigraphic units, hereafter referred as sedimentary Cycle-1, Cycle-2, and Cycle-3, respectively (Figs. 3–5). The general stratigraphy is shown in Figure 4A, and the schematic generalized vertical sections, together with the corresponding stick-logs for the northern and southern areas of the Kuh-e-Faghan Fault, are reported in Figure 5. The estimated thickness variations have been measured along seriate transects shown in Figure 3.

### Cycle-1

Cycle-1 consists of breccias (Ng-B) that distally evolve into crudely stratified conglomerates (hereafter referred to as Ng-C), which lie above a major angular unconformity (Fig. 4B) onto pre-Neogene rocks. Cycle-1 shows large lateral thicknesses variations. In particular, the basal talus Ng-B breccias occur only along the western part of the study area (Fig. 3). Their thickness varies strongly across strike of the Kuh-e-Faghan Fault from south to north, reaching up to ~450 m and ~100 m, respectively (Fig. 5). The overlying alluvial-fan conglomerates of Ng-C are thickest (~500 m) along the geological cross-section A-B (Fig. 3) but they more commonly do not exceed 300 m in thickness (Fig. 5).

The majority of the conglomerates and breccias are clast supported, but they transition into matrix-supported conglomerates in places in the upper part of the cycle. The matrix (up to 25%) is usually made of dark-red to pale-gray mudstone and siltstone. Clasts making up the bulk of the basal deposits have been directly sourced from the proximal pre-Neogene substratum. The clasts vary from boulder to cobble size. In places, the basal deposits include boulder (up to 1–3 $m^3$ in volume) deposits made of breccias and/or conglomerates, indicating reworking of the older part of Cycle-1. Here, we interpret these breccias (Ng-B) as talus deposits sourced by the local linear mountain ridge, whereas the Ng-C conglomerates are interpreted as alluvial-fan deposits. The transition to the upper part of Cycle-1 varies from gradual to sharp on an angular unconformity (Fig. 4B). Where basal breccias are absent, the upper part of Cycle-1 unconformably overlies the basement units, with deposits consisting of clast-supported, crudely to well-stratified polymictic conglomerates, with relatively rounded and sorted clasts. In places, imbricated clasts, arranged in 0.5–3.5-m-thick lenticular and, at times, laterally discontinuous beds, point to fluvial channel deposits.

According to differences in lithofacies from the upper part of Cycle-1, a distinction can be made between the western and eastern areas. Along the western area, the conglomerates generally exhibit less rounded and more chaotically organized clasts, with matrix-rich horizons showing convolute sedimentary structures. In contrast, along the eastern sector, the conglomerate deposits are typically interbedded with subordinate, fining-upward, 10–50-cm-thick sandstones packages. Concave-upward erosional surfaces and lenticular bed geometries are common. These differences in the Cycle-1 lithofacies could be related to the presence of a more unstable sedimentary basin linked to uplifting local source areas in the western part with respect to the eastern region of the study area.

Cycle-1 is interpreted as a high-energy deposit. The poorly sorted, texturally immature, and chaotic nature of the basal breccias, coupled with the clast lithology, all suggest very proximal deposition on steep slopes by block fall and in proximal fans and/or as talus cones. The laterally continuous nature of the upper part of Cycle-1 deposits also suggests that deposition occurred within an alluvial-fan complex in the west area and a broad, well-fed alluvial plain to the east.

**Figure 4 (*on following page*). (A) Panoramic view showing the three Neogene sedimentary cycles and their stratigraphic relations. Contacts between Cycle-1 and Cycle-2 deposits are bounded by a steeply dipping fault zone (fault trace indicated by black arrows). View looking northward; length of the stratigraphic section ~4 km. (B) Panoramic view of Cycle-1 deposits onlapping onto the Paleozoic and Mesozoic basement. Note the angular contact between the basal breccias (Ng-B) and the upper Ng-C fluvial conglomerates. The inserts show the characteristic sedimentary structures of the deposits. Cycle-3 onlaps directly onto Cycle-1. (C) Progressive angular unconformities within Cycle-2. The inserts show the range of sedimentary structures observed within Cycle-2, attesting to its fluvio-palustrine depositional environment. (D) Panoramic view showing Cycle-3 onlapping directly onto the Paleozoic and Mesozoic basements units. Bedding strike and dip measurements are marked by white dots. The inserts show the range of sedimentary structures observed within the basal unit of Cycle-3, attesting to its lacustrine/playa lake depositional environment. The white dotted line shows the contact between Neogene sediments and basement units. In all figures, the white dots indicate points of bedding attitude measurements (in degrees, right-hand rule).**

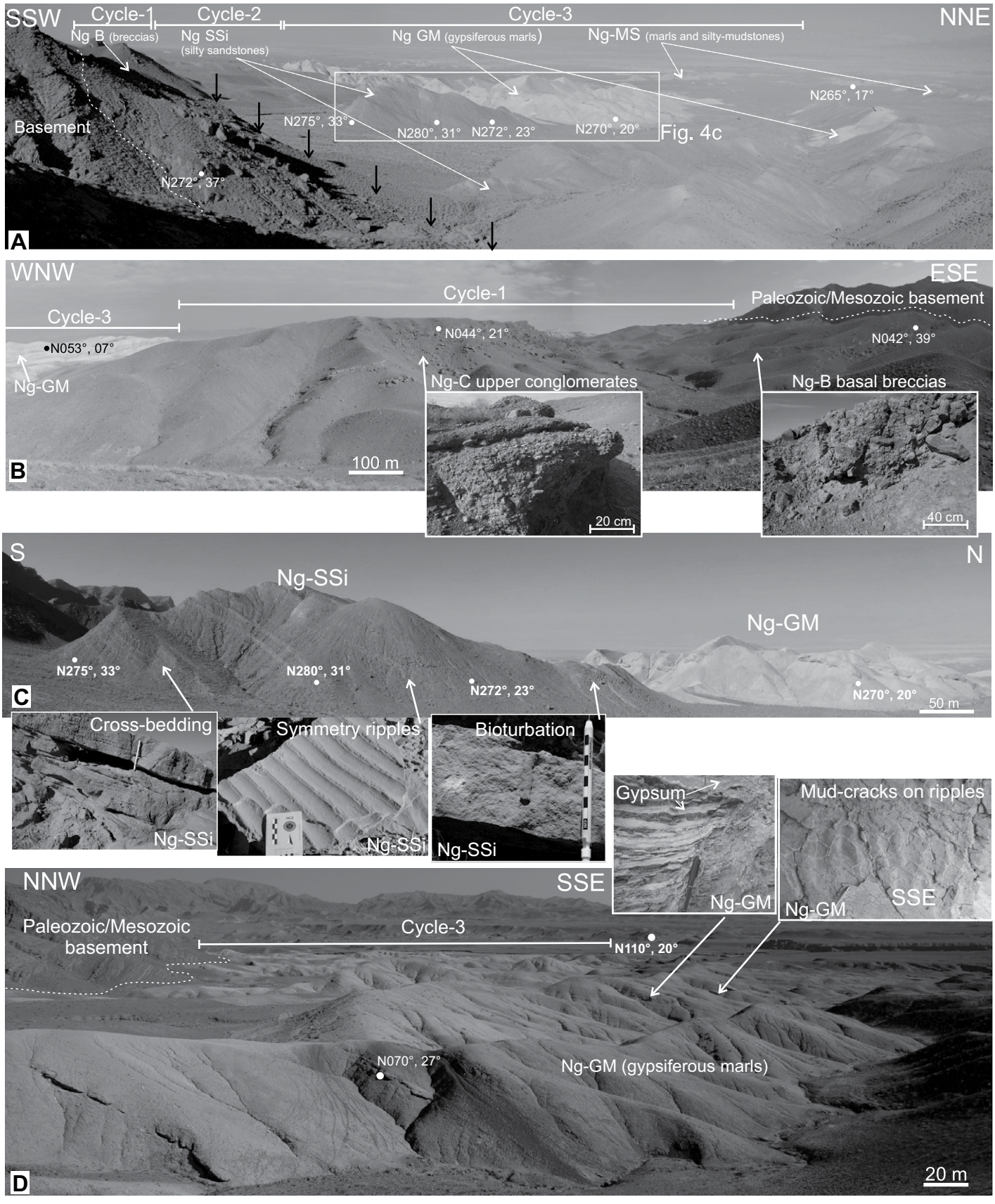
SSW
Cycle-1
Cycle-2
Cycle-3
NNE
Ng B (breccias)
Ng SSi
(silty sandstones)
Ng GM (gypsiferous marls)
Ng-MS (marls and silty-mudstones)
Basement
N275°, 33°
N280°, 31°
N272°, 23°
N270°, 20°
N265°, 17°
Fig. 4c
N272°, 37°
A
WNW
ESE
Cycle-1
Cycle-3
Paleozoic/Mesozoic basement
N044°, 21°
N042°, 39°
N053°, 07°
Ng-GM
Ng-C upper conglomerates
Ng-B basal breccias
100 m
20 cm
40 cm
B
S
N
Ng-SSi
Ng-GM
N275°, 33°
N280°, 31°
N272°, 23°
N270°, 20°
50 m
C
Cross-bedding
Ng-SSi
Symmetry ripples
Ng-SSi
Bioturbation
Ng-SSi
Gypsum
Ng-GM
Mud-cracks on ripples
Ng-GM
SSE
NNW
SSE
Paleozoic/Mesozoic basement
Cycle-3
N110°, 20°
N070°, 27°
Ng-GM (gypsiferous marls)
20 m
D

**Figure 4.**

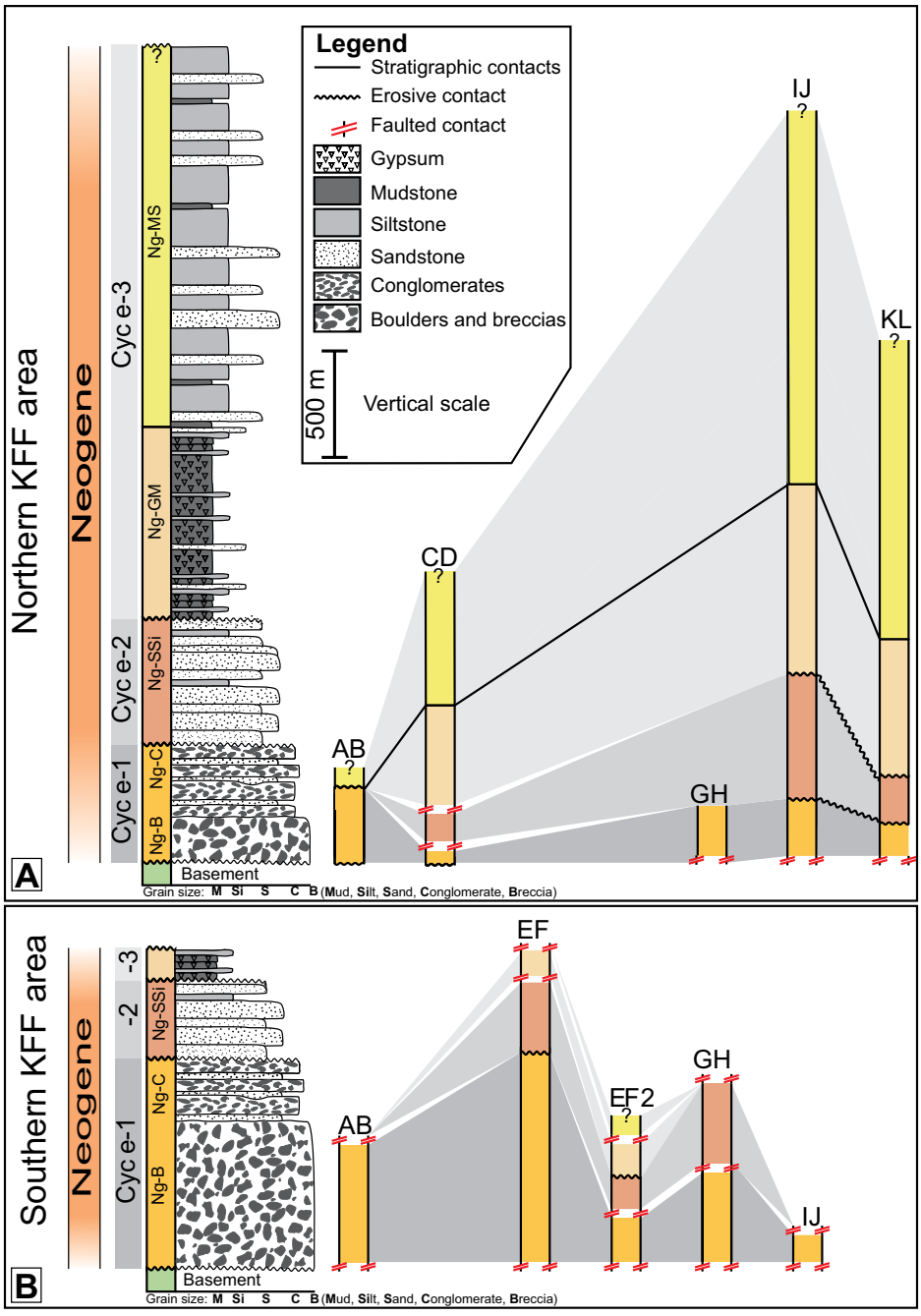


**Figure 5. Generalized vertical stratigraphic section (GVS) of the Neogene deposits for the northern (A) and southern (B) sectors of the study area. The series of stick-logs report the unit thicknesses measured along the relative geological transects (AB, CD, EF, EF2, GH, IJ, KL) shown in Figure 3. Scale and legend in A apply to both figures. KFF—Kuh-e-Faghan Fault.**

### Cycle-2

Cycle-2 consists of decimeter-thick, bedded, well-sorted, mineralogically and texturally immature, medium to coarse silty red sandstone (hereafter referred to as Ng-SSi). Cycle-2 is absent in the westernmost part of the Kuh-e-Faghan Fault and generally increases in thickness eastward, where it reaches its maximum (~580 m) along geological transects G-H and I-J (Figs. 3 and 5). Progressive angular unconformities affecting those continental deposits are very common, especially in the lower part of Cycle-2 (Fig. 4C).

Cycle-2 Ng-SSi usually shows planar- to cross-lamination and unconformably covers the Ng-C deposits. In places, the Ng-SSi deposits are characterized by trough cross-bedding alternating with subordinate horizons of coarse gravelly sandstones. Straight-crested symmetric, lunate, and linguoid ripples are all common features of the Cycle-2 deposits, together with locally bioturbated horizons and surfaces exhibiting mud cracks and casts (Fig. 4C), which represent the channel/bank and overbank deposits, respectively.

We interpret Cycle-2 deposits as related to a fluvio/palustrine environment, possibly proximal to a wide, well-fed alluvial plain capable of being supplied by relatively well-sorted material. The close proximity of the source produced mineralogically and texturally mature sediments.

### Cycle-3

Cycle-3 deposits form two distinct units, Ng-GM and Ng-MS (Figs. 3, 4D, and 5). The basal unit Ng-GM shows a distinct angular unconformity at the base (Fig. 4D), and it consists of a marly succession and subordinate gypsum horizons. It is absent in the western part of the Kuh-e-Faghan Fault, and it reaches its maximum thickness (~450 m; Figs. 3 and 5) in the central sector of the study area and then thins out eastward. Some fine sandstone beds, tens of centimeters thick, are also present, with infrequent planar- to cross-laminated horizons. Desiccation cracks and mud casts are also common (Fig. 4D). The gypsum horizons, up to a few tens of centimeters thick, are typically secondary, showing a displacive character of the gypsum crystals, which also occur along bedding surfaces and fractures. In places, this secondary origin for the gypsum layers is responsible for the deformation and disruption of the original layering. The basal and upper parts of the Ng-GM unit are characterized by meter-thick red marls and silts, relatively free of gypsum, interbedded with pale-yellow gypsiferous silty marls, while the central portion is characterized by continuous thick packages of pale-yellow gypsiferous silty marls.

The subsequent Ng-MS unit conformably overlies Ng-GM deposits. It consists of a few tens of centimeters of pale-red to beige, massively bedded marls and silty mudstones, with millimeter-scale layering. These are interbedded with subordinate 0.5–2.5-m-thick cross-bedded, at times laterally discontinuous, light-brown, medium to coarse sandstones. Bedding surfaces exhibiting small-scale straight-crested asymmetric ripples are uncommon but not rare. The Ng-MS unit extends throughout the northern

Kuh-e-Faghan Fault area, reaching a maximum thickness of ~1230 m (transect IJ in Fig. 3; see also Fig. 5).

The Ng-GM unit is inferred to have been deposited under different climate conditions, ranging from dry episodes, characterized by evaporation-dominated events (secondary gypsum grew within sediments), to wetter conditions, indicated by suspension-dominated deposits (massive and layered marls and silty-mudstones) or deposits formed in an environment with a relatively high-energy tractional and unidirectional turbulent flow (rippled silty marls and fine sands). Such sedimentary characteristics are representative of playa mud flats and playa lake environments (Reading, 2009). The marls and silty mudstones of the Ng-MS unit, mainly characterized by millimeter-scale layering and some rare rippled surfaces, are indicative of deposition in a wet period from a low-energy shallow lacustrine environment, where deposition occurred primarily by suspension settling and secondarily by laminar and turbulent flow. The subordinate meters-thick cross-bedded sandstone was deposited by more turbulent and energetic flow and represents deposition during periods of increased sediment supply from riverine input.

## STRUCTURE

The basement units exhibit a steeply dipping, ENE-WSW–oriented planar fabric, similar to the neighboring Kuh-e-Sarhangi fault system (Nozaem et al., 2013). The Neogene deposits show bedding attitudes dipping away from, and striking subparallel to the axis of the topographic divide, arranged to form a broad eastward-plunging anticline. Moreover, the bedding dip angle of the Neogene deposits generally decreases away from the boundary fault system (see the geological map in Fig. 3).

The Kuh-e-Faghan Fault system consists of three, fault strands: the broadly left-stepping, E-W–striking (1) western and (2) central fault strands that abut the (3) NW-SE– to E-W–striking eastern fault strand (Fig. 3). The fault strands have along-strike lengths of 30–40 km, and their associated fault damage zones bound E-W elongated ridges. We measured 501 striated fault surfaces (over a total number of 1040 structural data) occurring in the basement units, the Neogene and Quaternary deposits. Fault kinematics were obtained based on classical criteria for brittle shear zones, such as fault offset, growth fibers, and Riedel shears (Petit, 1987; Doblas, 1998). Fault orientation analysis was performed using the software Daisy 3 (Salvini, 2004; http://host.uniroma3.it/progetti/fralab). The faults show high- to subvertical dips, with a maximum frequency distribution at 85° and a mean dip value of 75°. The fault strikes show a maximum at N94°, with subordinate N131° and N47°. The frequency distribution of the pitch angle (counted positive in the plane from the fault strike) of the measured slickenlines shows dominant strike-slip kinematics with maxima at 12° and 162° and a subordinate dip-slip population (84°). In particular, the analysis shows that ~72% of the slickenline pitches are in the ranges 0°–45° and 135°–180°, and less than 28% exhibit 45° to 135° pitches. The mean pitch values is 2° (see inset in Fig. 3).

In the following sections, a systematic description of the fault system geometry and kinematics along the main fault strands is provided.

### Western Fault Strand

The western fault strand runs W-E for more than 35 km on the southern side of the Kuh-e-Faghan Fault, with variations along strike (Fig. 3). The western fault tip is defined by a broad (wavelength of ~5 km), E-W–striking, south-verging monocline that affects the basal Ng-C deposits. The fold axial trace maps out ~20 km and separates gently north-dipping (<20°) strata to the north from steeply south-dipping (>40°) strata to the south, narrowing to the east (Fig. 3). The fault plane rarely cuts through Ng-C strata, and therefore the fault is considered as mostly blind (Fig. 3). Moving eastward along the western fault strand trace, the southern limb of the monocline becomes increasingly steeper to overturned and is dissected by numerous subvertical fault strands (see the geological cross-section A-B in Fig. 3 and Fig. 6A). These fault strands define an ~50-m-wide fault damage zone, made of vertical, E-W–striking fractured rock panels along which abrupt contacts between the basal Neogene conglomerates (Ng-C) and the gypsiferous marls (Ng-GM) occur (Fig. 6A). Shearing is dominantly localized along E-W–striking dextral slip zones, associated with smaller synthetic NW-SE–striking faults (stereoplot in Fig. 6A).

Further to the east, the western fault strand bends NE to form a major restraining bend that affects the Neogene deposits, with positive flower structures in cross section and a contractional strike-slip duplex (Woodcock and Fischer, 1986) in map view (see geological cross-sections E–F and E2–F2 in Fig. 3). The duplex-bounding faults are developed within the Neogene deposits; however, faults also affect the Quaternary alluvial deposits (see following). The restraining bend is associated with development of a tight NE-SW–trending syncline, mapping out subparallel to the main fault trace and affecting the Ng-C and the unconformable Ng-SSi deposits. The fold profile shows a moderately north-dipping southeastern flank with a steep to overturned northwestern flank, with a periclinal doubly plunging geometry (Fig. 3). The northwestern fold limb is dissected by NE-striking subvertical fault strands that cause the tectonic repetitions among the Neogene units. The duplex-bounding faults are subvertical, with fault slip localization occurring along the northwestern boundary fault zone. This fault zone consists of an ~300-m-wide damage zone, defined by subvertical panels of cataclastic fault rocks and cohesive fault breccias (Fig. 6B). Dextral kinematics are attested by drag folding of the Neogene strata along the principal displacement zone (Fig. 6C). Measured fault surfaces strike NE-SW; offset bedding truncations, Riedel shears, and calcite slickenfibers systematically document either dextral oblique strike-slip or reverse kinematics (stereoplot in Fig. 6C).

### Central Fault Strand

The central fault strand runs W-E for ~30 km on the northern side of the Kuh-e-Faghan Fault, defining a sharp break in slope between the topographically elevated pre-Neogene substratum and the Neogene–Quaternary sedimentary covers (Fig. 3). Basement-cover relations are well preserved in the central part of the central fault strand, with fault zone localization occurring within the basement units and only marginally within the Neogene deposits (Ng-C and Ng-GM; cross-sections A-B and C-D in Fig. 3). In the field, they generally appear as broad (up to 100 m wide) deformation zones, associated with vertical rock panels affected by diffuse brittle deformation. The shear deformation is principally accommodated within the weaker basement shale beds, while the stronger sandstones remain partially coherent to define fault lithons (Fig. 7A). The slip zones are typically delocalized and defined by bands of cataclastic material meters to tens of meters thick. As in the western fault strand, well-developed fault surfaces with striations and kinematic indicators occur, but localized slip zones and fault gouges are rarely exposed. Brittle deformation in the Ng-C deposits is characterized by a dominant set of subvertical E-W–striking cataclastic zones, generally less than 1 m thick. Striated fault surfaces provide subhorizontal pitch values, and the fault kinematics are systematically dextral. Subsidiary, steeply dipping, NW-SE dextral and NNE-SSW sinistral faults are also reported (see the stereoplot in Fig. 7A).

Continuing to the east, the central fault strand bends southward and branches out into

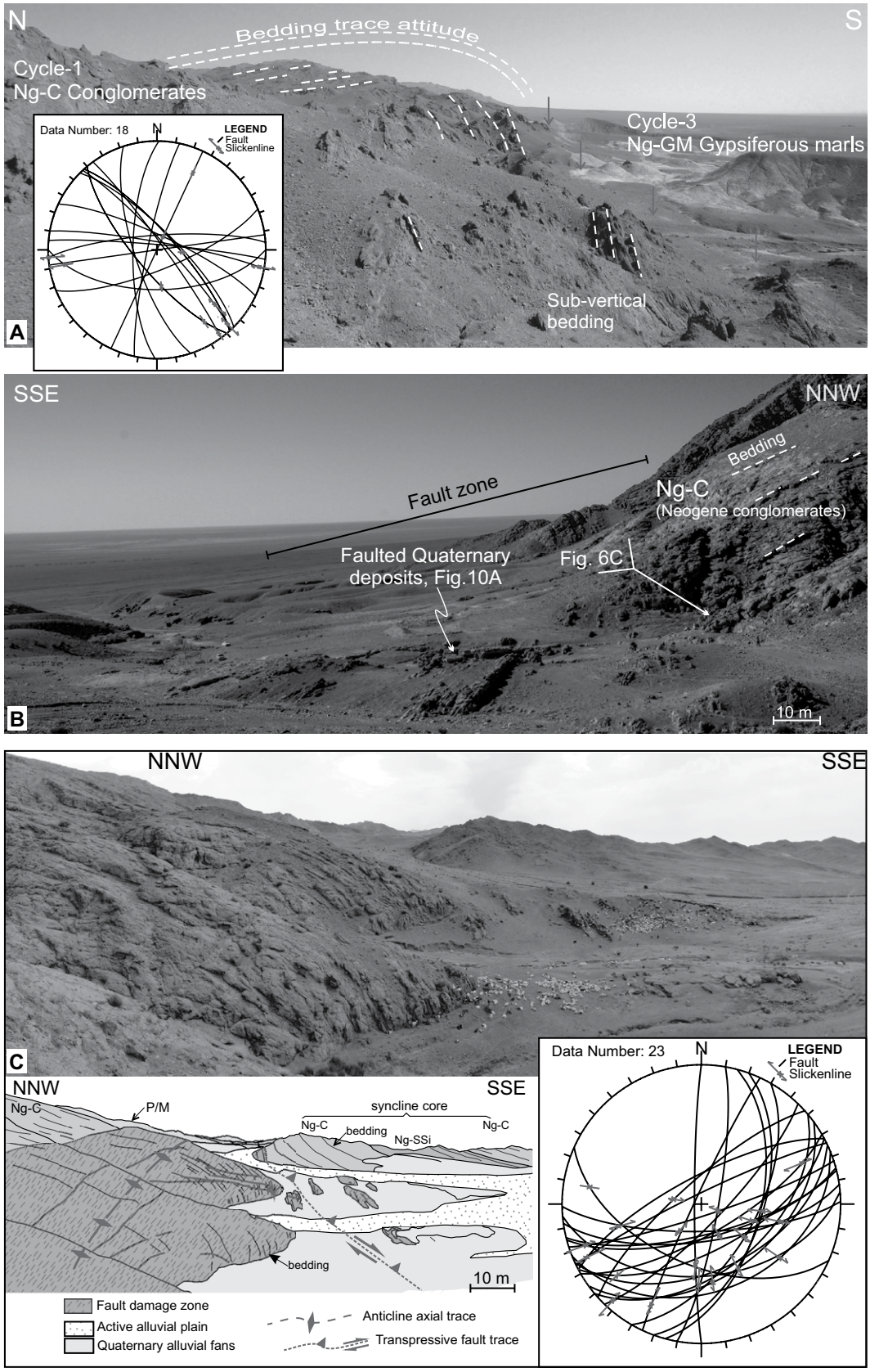


**Figure 6. Structures along the western fault strand. (A) Panoramic view (looking eastward), showing the core of the antiformal structure defined by the structural arrangement of the Cycle-3 Neogene conglomerates (Ng-C; field of view = 500 m). Note steepening of the southward limb approaching the western fault strand trace (gray arrows). The fault zone is defined by verticalized panels of cataclastic conglomerates (Ng-C) in tectonic contact with the Cycle-3 gypsiferous marls (Ng-GM). The stereoplot (Schmidt net, lower-hemisphere projection) details the collected fault data set (the longer arrow indicates the hanging-wall direction of slip, and its length relates to the horizontal component of slip; double half arrow indicates the sense of the strike-slip component). (B) The eastward termination of the western fault strand. Panoramic view (looking westward), showing the subvertical, ~400-m-thick damage zone associated with the NE bending of the western fault strand, which abruptly interrupts the monoclinal attitude of the Ng-C deposits. The fault zone involves the Quaternary alluvial and terraced deposits. (C) Hectometer-scale drag folding affecting the Neogene deposits when approaching the trace of the western fault strand and interpretative line drawing (for lithological symbols, see Fig. 3). The anticline is E/SE-plunging with an axial trace at an angle to the fault trace. Stereoplot (Schmidt net, lower-hemisphere projection) shows the collected fault data. Fault slip is dominated by dextral and reverse kinematics along NE-SW–striking, steeply dipping fault strands. See Figure 3 for location of the field pictures.**

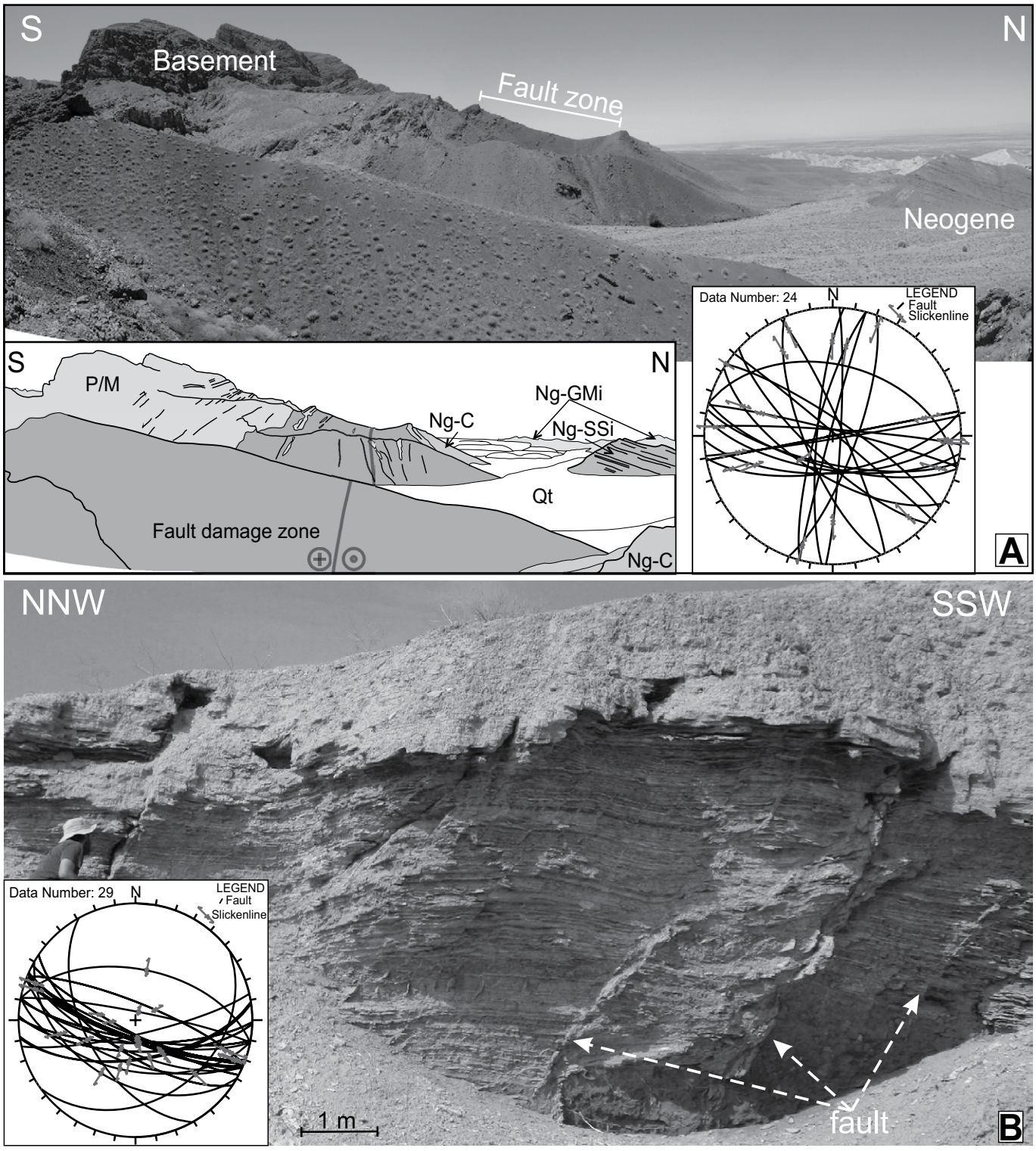


**Figure 7. Structures along the western fault strand. (A) The basement-Neogene fault contact along the western tip of the central fault strand (looking westward) and interpretative line drawing (for lithological symbols, see Fig. 3), showing the fault zone architecture and fault zone localization along the verticalized weaker basement shale units. The stereoplot details the collected fault data set (Schmidt net, lower-hemisphere projection). (B) Mesoscale NW-SE–striking fault systems in the Ng-GM deposits along the eastward termination of the western fault strand. Note the synsedimentary character of faulting: the faults die out upward into the sediments. The stereoplot (Schmidt net, lower-hemisphere projection) details the collected fault data set (the longer arrow indicates the hanging-wall direction of slip, and its length relates to the horizontal component of slip; double half arrow indicates the sense of the strike-slip component). WNW-ESE dextral and oblique (transtensional)- and normal-slip faults are observed. See Figure 3 for location of field pictures.**

four main NW-SE–oriented subvertical fault segments, which in map view are arranged to form a 10-km-wide, trailing extensional imbricate fan (Woodcock and Fischer, 1986), also referred as to "horsetail-type" transtensive termination (Fig. 3; Granier, 1985). The dominant strike-slip motion along the central fault strand passes into a lozenge-shaped zone of extension or transtension at its tip, consistent with dextral offset, which is filled up by the Ng-GM deposits (Fig. 3). Striated fault surfaces either show dip-slip normal or oblique-to-strike-slip dextral kinematics. Faulting within the Ng-GM deposits is accommodated by diffuse zones of deformation, hundreds of meters wide, characterized by evenly spaced (meters apart) sets of NW-SE–striking faults that accommodate both oblique-slip and normal dip-slip displacements. Many of these mesoscale faults show offsets that die out upward, and some of them die out vertically, indicating syndepositional faulting (Fig. 7B).

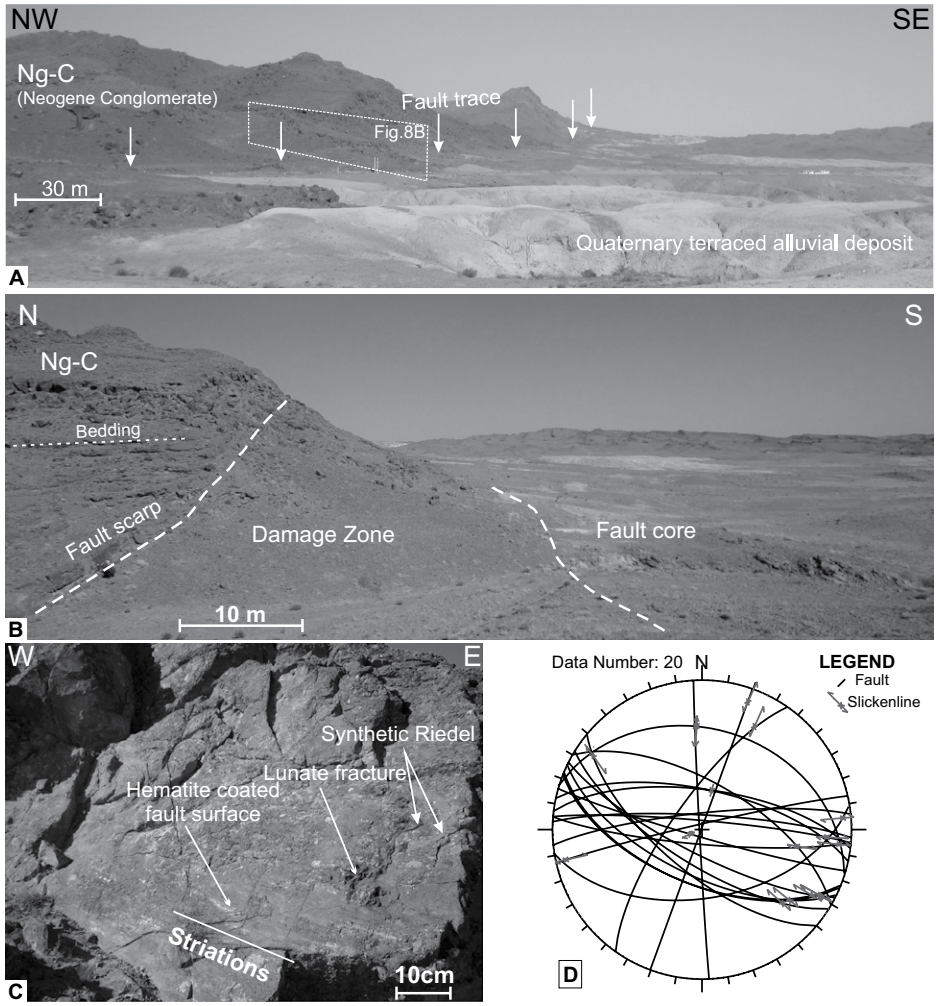


**Figure 8. (A) Panoramic view (looking northeastward) of the prominent break in slope that defines the trace of the eastern fault strand, bounding Neogene (Ng-C) and Quaternary deposits. (B) Structural architecture of the fault zone across the eastern fault strand, exhibiting pluridecameter-thick, subvertical damage zone and fault core. The stereoplot (Schmidt net, lower-hemisphere projection) shows the collected fault data set (the longer arrow indicates the hanging-wall direction of slip, and its length relates to the horizontal component of slip; double half arrow indicates the sense of the strike-slip component). Faulting is dominated by WNW-ESE–striking dextral faults associated with minor antithetic NNE-SSW–striking sinistral ones. (C–D) Examples of polished, E-W–striking, hematite-coated fault surfaces, exhibiting prominent subhorizontal striations. The kinematic indicators as provided by synthetic Riedel shears, lunate fractures, and abrasion steps attest to dextral kinematics. See Figure 3 for location of field pictures.**

### Eastern Fault Strand

The eastern fault strand is an ~40-km-long, subvertical fault zone made of the coalescence of several synthetic faults to form a curvilinear slip zone and prominent range front, striking from NW-SE to E-W at its eastward termination (Fig. 3). The fault zone shows a decameter-to-hectometer-thick damage zone that consists of numerous mesoscale fault segments cutting through the pre-Neogene basement units that are tectonically juxtaposed against the Ng-GM successions. In particular, the NW segment abruptly cuts an E-W–striking Neogene basin boundary fault strand. It continues eastward bending to E-W direction, showing a prominent linear fault scarp in the Neogene deposits that can be traced continuously eastward for more than 20 km in the Quaternary alluvial plain (Fig. 8A). Where the fault zone bends to an E-W direction, the fault damage zone widens to more than 200 m wide and has prominent fault cores, up to tens of meter thick. The fault cores consist of ultracataclastic bands and fault gouges, separated by brecciated fault rocks and sheared lithons (Fig. 8B). Major fault surfaces are typically subvertical, NW-SE and E-W striking, and exhibit subhorizontal slickenlines (pitch: 5°–15°). Most of the striated fault surfaces have hematite coatings. Fault kinematics as deduced by synthetic Riedel shear planes, together with calcite slickenfibers, grain grooves, and lunate fractures systematically point to dominantly dextral slip (Figs. 8C–8D). Decameter-scale S-C fabrics are observed along coherent tracts of the principal displacement zone of the eastern fault strand and continue over significant distances (>300 m), both along the basement-Neogene contacts and within the Neogene deposits (Figs. 9A–9B). Within these deformation zones, S surfaces are defined by dissolution seams and strike NW-SE, and the C surfaces strike roughly E-W to ENE-WSW. Lineations are provided by slickenlines on the C surfaces that systematically are subhorizontal. The S-C fabrics are associated with NW-SE–striking, steeply dipping joint and calcite- and gypsum-bearing vein sets, indicating dextral shearing (Fig. 9C). Meter-thick cohesive and foliated cataclasites are observed in places to form the fault rocks along the slip zones developed within the Neogene deposits.

### Quaternary Faulting

The Quaternary successions along the Kuh-e-Faghan Fault consist of a wide variety of alluvial-fan and fluvial deposits, made of conglomerates, gravels, and sands exhibiting various degrees of consolidation. These deposits lie upon a regional erosional surface (pediment) cut through the

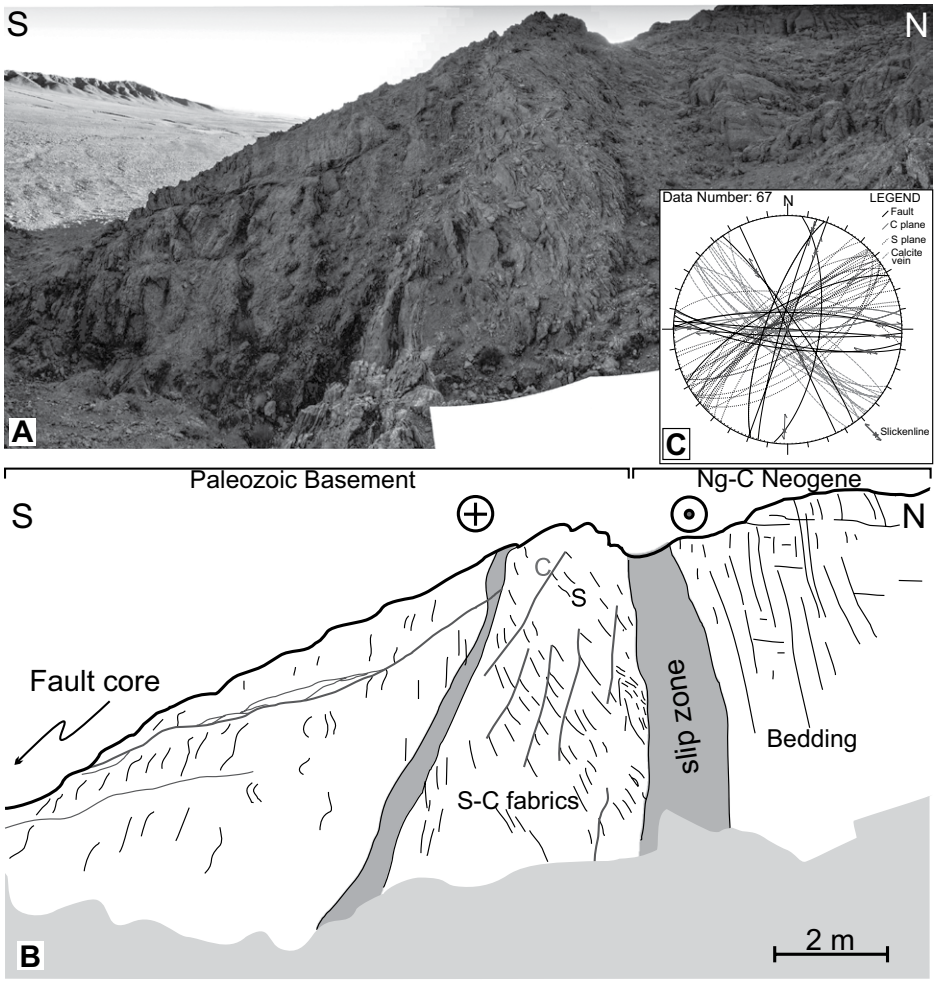


**Figure 9. (A) Outcrop-scale picture and (B) schematic line drawing showing S-C tectonites developed along the main trace of the eastern fault strand bounding the basement-Neogene (Ng-C) contact (for location of field picture, see Fig. 3). Note the occurrence of meter-thick, E-W–striking subvertical ultracataclastic dextral slip zones that bound the main fault rock types. (C) Stereoplot (Schmidt net, lower-hemisphere projection) showing the angular relationships between the S-C fabrics, the vein array, and the main strike-slip fault surfaces. In the stereoplot, the longer arrow indicates the hanging-wall direction of slip, and its length relates to the horizontal component of slip. Double half arrow indicates the sense of the strike-slip component.**

strongly tilted Neogene units (Figs. 6B and 8A). Quaternary faults and joints occur along the western fault strand and the eastern fault strand (see Fig. 3 for site locations), where faulting is dominated by dextral fault zones.

Along the contractional bending at the eastern end of the western fault strand, dextral and oblique-slip faults cut through the Quaternary terraced deposits, juxtaposing and squeezing together lenses of Quaternary and Neogene sediments (Figs. 10A–10B). Such faults show transpressive dextral kinematics, compatible with faulting in the Neogene deposits (Fig. 10C).

Along the eastern fault strand, Quaternary faulting is documented both along the principal displacement zone and along subsidiary, synthetic fault strands (Fig. 3). Along the prominent E-W–striking fault scarp that defines the geomorphic expression of the eastern fault strand (Fig. 8A), Quaternary deposits are extensively affected by a set of subvertical joint arrays. Further to the east, along the NW-SE fault systems that make up the transtensional trailing-end imbricate fan of a major dextral fault segment to the north of the eastern fault strand, extensional and dextral oblique-slip faults involve the Ng-GM deposits and the Quaternary alluvial cover (Fig. 3). Evidence of Quaternary faulting is documented along an E-W–striking minor fault strand. In this area, E-W–oriented subvertical faults cut through the gypsiferous Neogene units and into the Quaternary alluvial deposits, displaying calcite slickenlines and small-scale drag folding, compatible with dextral kinematics (Figs. 10D–10E).

## AHe THERMOCHRONOMETRY

The low closure temperature for the apatite (U + Th)/He system (65–70 °C for typical rates of cooling and grain sizes; Farley, 2000) makes it particularly useful for assessing the ages of the late-stage deformation and exhumation history affecting the uppermost portions of the crust, where brittle deformation and faulting predominate.

Samples from the basement units ($n$ = 6) and basal Neogene deposits (Ng-C and Ng-SSi units; $n$ = 11) were collected for AHe thermochronometry along an approximately constant elevation transect parallel to the Kuh-e-Faghan Fault trace (mean altitude of 1070 m; Fig. 11). The samples are from the sandstone portions of the Paleozoic and Mesozoic deposits and the Neogene basal sandy intercalations of Cycle-1 and Cycle-2. The quantity and quality of apatite grains are highly variable. In most of the samples, apatite grains appear rounded with frosted surfaces, making the identification of inclusion-free grains difficult. Consequently, eight samples were excluded from the analysis due to their poor apatite quality (Fig. 11).

The analytical protocol adopted in this study follows Foeken et al. (2006, 2007). Refer to the Appendix for methods and analytical procedure. Single-grain ages corrected for α-ejection (Farley et al., 1996) generally show a good within-sample reproducibility (Table 1). Mean ages and standard deviations are plotted in Figure 11. Three samples show single grain ages that do not overlap within two standard deviations with the other ages of the same sample. Because these three grains have low U and Th contents, we consider them as outliers, and they were not included in the mean age calculation. All samples have mean and single-grain AHe ages that are younger than the stratigraphic age, indicating that all were reset. The ages indicate a Miocene to Pliocene cooling/exhumation history. Mean ages range from 2.9 ± 1.5 Ma to 20 ± 2.6 Ma and define two mean age populations, clustering at ca. 18 and ca. 4 Ma (Table 1).

The spatial distribution of the AHe ages shows two broad areas: (1) the western area, consisting of the topographically prominent fault-bounded basement high to the west of the eastern fault strand, where cooling ages are older; and (2) the eastern area, located alongside of the eastern fault strand, where cooling ages

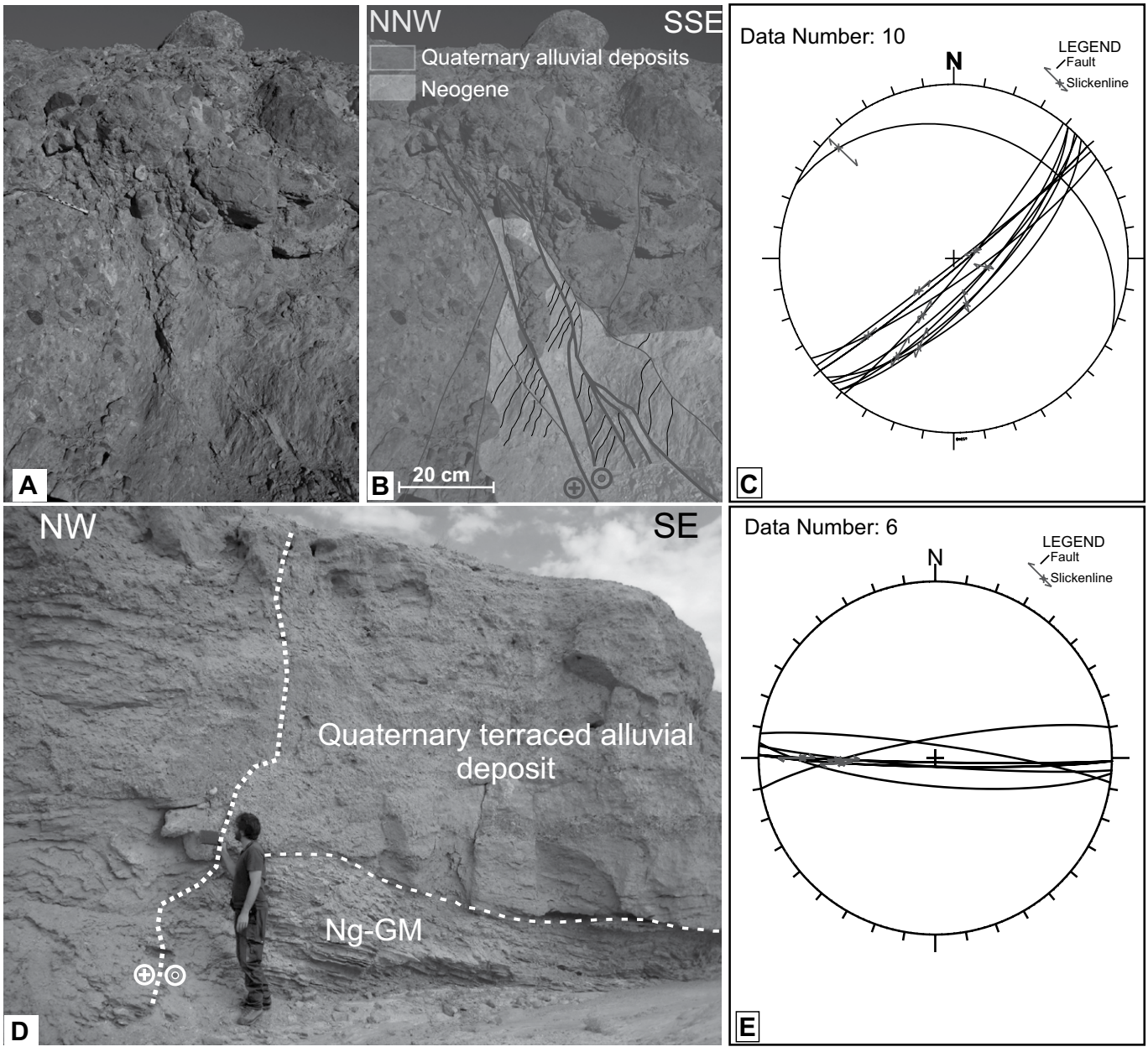


**Figure 10. Quaternary faults. (A) Outcrop picture and (B) line drawing showing fault strands cutting though the Neogene (Ng-C) and the overlying Quaternary alluvial deposits shown in Figure 6B. (C) Stereoplot showing the collected fault data (Schmidt net, lower-hemisphere projection) set in the locality of Figure 10A. The faults strike NE-SW and show dextral and reverse kinematics. Steeply dipping, NE-SW dextral and reverse faults cut through and involve Neogene and Quaternary deposits. (D) E-W–striking dextral fault cutting through alluvial Quaternary deposits overlying Cycle-3 gypsiferous marl (Ng-GM) deposits. (E) Stereoplot showing the collected fault data set (Schmidt net, lower hemisphere projection) in the locality of Figure 10D. In the stereonet, the longer arrow indicates the hanging-wall direction of slip, and its length relates to the horizontal component of slip. Double half arrows indicates the sense of the strike-slip component. See Figure 3 for location of field pictures.**

are younger (Fig. 11). The AHe age distribution in the western area shows that the basement bedrock experienced a similar exhumation and cooling history during and since the early Miocene, ca. 18 Ma, with the exception of sample IR-10, which exhibits a cooling age of ca. 3 Ma. The AHe ages from the eastern area are systematically younger, clustering at ca. 4 Ma. This pattern is not uniform, as sample IR-17, from the pre-Neogene basement, shows an age of ca. 8 Ma. The distribution of AHe ages indicates a pattern that may relate to differential exhumation/cooling history along the strike of the Kuh-e-Faghan Fault.

## DISCUSSION

The multidisciplinary data set presented in this study gives spatial and temporal constraints on the geological history and evolution of the Kuh-e-Faghan Fault system (Fig. 1). By linking structures, stratigraphy, and apatite thermo-

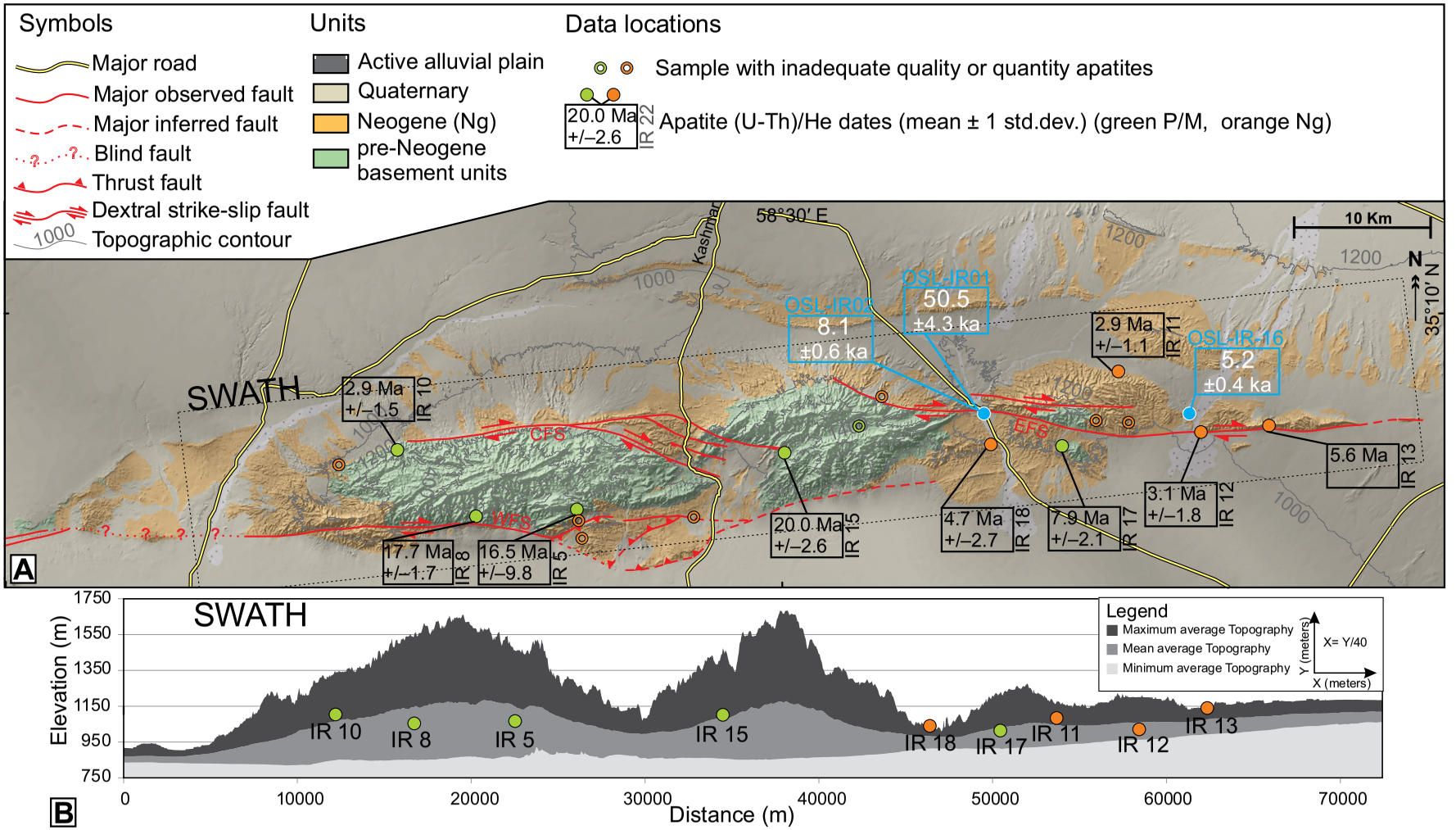


**Figure 11. (A) Structural map of the Kuh-e-Faghan Fault on shaded topographic elevation model, showing the locations of the samples used for AHe thermochronometry, together with mean age results from each sample indicated (see Table 1). (B) Distribution of AHe sample elevations and ages projected onto an along-strike topographic SWATH profile (40 times vertical exaggeration) along the Kuh-e-Faghan Fault. WFS—western fault strand; EFS—eastern fault strand; CFS—central fault strand.**

chronometry to the long-term response to crustal deformation in intraplate settings, the results may elucidate the way strike-slip faulting nucleates and propagates.

## Structural Synthesis

The geological investigation shows that the Kuh-e-Faghan Fault consists of three main, left-stepping, dextral fault strands that cut through the Paleozoic and Mesozoic basement units and the Neogene-Quaternary sedimentary cover (Fig. 3). The fault zones are tens of kilometers long and cut at high angle the NE-SW–striking planar fabrics of the basement rocks (Fig. 3), ruling out a major contribution of tectonic reactivation during Kuh-e-Faghan Fault development.

The dextral fault population (261 of 501 data) provides a mean strike cluster at N91°. This is interpreted as the strike of the principal displacement zone of the Kuh-e-Faghan Fault. The normal fault and extensional vein strike data ($n$ = 111) have strike clustering at N135°. These angular relationships suggest fault zone development in response to a (local) regional direction of the maximum principal stress ($R\sigma_1$) trending NW-SE, at an angle of ~44° from the principal displacement zone. This implies simple shear–dominated strike-slip deformation (simple shear wrenching in Fossen et al., 1994) during Kuh-e-Faghan Fault development, in agreement with the mean pitch angle (2°) of the fault slickenlines as obtained from the cumulative fault data set (see Fig. 3). Within this scenario, the along-strike spatial variation of the fault orientations, kinematics, and strain regimes (restraining and releasing areas) reflect the different ways by which the overall E-W right-lateral shear is accommodated, distributed, and partitioned along the principal and minor fault strands of the Kuh-e-Faghan Fault system (Fig. 3).

Fault zone geometry and structural characteristics vary along strike. There is an eastward increase in shear localization within the main fault zones, from distributed deformation characterized by cataclastic fault rocks in the west (the western fault strand and central fault strand) to localized and mature fault zones characterized by ultracataclastic fault gouges (distributed cataclastic flow) and S-C fabrics in the east (the eastern fault strand). Porous rocks such as those making up the basal deposits of the faulted Neogene strata along the Kuh-e-Faghan Fault display a transition from dilatant, brittle behavior to shear-enhanced compaction and macroscopically ductile behavior with increasing effective pressure at constant temperature (Rutter and Hadizadeh, 1991; Scholz, 2002; Paterson and Wong, 2005; Wong and Baud, 2012). This is documented along the Kuh-e-Faghan Fault by

TABLE 1. APATITE (U-Th)/He DATA

| Sample | Rock unit | Location | | Altitude (m) | Sample no. | U (ng) | Th (ng) | He (cc) | He age (Ma) | Ft | Corrected He age (Ma) | Uncertainty | Mean age | Uncert st. dev. |
|---|---|---|---|---|---|---|---|---|---|---|---|---|---|---|
| | | Lat (°N) | Long (°E) | | | | | | | | | | | |
| IR-8 | Pre-Neogene | 35.060867 | 58.316167 | 1054 | IR-8.1 | 0.0166 | 0.106 | 2.91E−11 | 5.44 | 0.77 | 7.1* | 0.2 | 17.7 | ±1.7 |
| | | | | | IR-8.2 | 0.0124 | 0.189 | 9.23E−11 | 12.81 | 0.73 | 17.5 | 0.4 | | |
| | | | | | IR-8.3 | 0.0627 | 0.248 | 1.71E−10 | 11.38 | 0.74 | 15.4 | 0.3 | | |
| | | | | | IR-8.4 | 0.297 | 0.507 | 7.62E−10 | 14.95 | 0.77 | 19.5 | 0.4 | | |
| | | | | | IR-8.5 | 0.212 | 0.559 | 6.01E−10 | 14.26 | 0.77 | 18.4 | 0.4 | | |
| IR-15 | Pre-Neogene | 35.096801 | 58.494049 | 1102 | IR-15.1 | 0.059 | 0.392 | 2.30E−10 | 12.30 | 0.71 | 17.4 | 0.4 | 20.0 | ±2.6 |
| | | | | | IR-15.2 | 0.031 | 0.139 | 6.89E−11 | 8.53 | 0.77 | 11.1* | 0.3 | | |
| | | | | | IR-15.4 | 0.227 | 2.591 | 1.91E−09 | 18.66 | 0.83 | 22.6 | 0.5 | | |
| | | | | | IR-15.5 | 0.044 | 2.496 | 1.37E−09 | 17.77 | 0.89 | 20.0 | 0.5 | | |
| IR-10 | Pre-Neogene | 35.095326 | 58.254287 | 1104 | IR-10.1 | 0.001 | 0.302 | 4.21E−12 | 0.46 | 0.64 | 0.7* | 0.3 | 2.9 | ±1.5 |
| | | | | | IR-10.2 | 0.009 | 0.105 | 1.21E−11 | 2.78 | 0.72 | 3.9 | 0.2 | | |
| | | | | | IR-10.3 | 0.003 | 0.125 | 5.03E−12 | 1.19 | 0.67 | 1.8 | 0.2 | | |
| IR-11 | Neogene deposits | 35.132007 | 58.688542 | 1084 | IR-11.1 | 0.003 | 0.056 | 5.09E−12 | 2.28 | 0.64 | 3.6 | 0.3 | 2.9 | ±1.1 |
| | | | | | IR-11.2 | 0.003 | 0.049 | 4.60E−12 | 2.20 | 0.63 | 3.5 | 0.3 | | |
| | | | | | IR-11.3 | 0.004 | 0.033 | 1.72E−12 | 1.02 | 0.64 | 1.6 | 0.8 | | |
| IR-13 | Neogene deposits | 35.100512 | 58.673708 | 1140 | IR-13.1 | 0.005 | 0.081 | 1.34E−11 | 4.18 | 0.74 | 5.6 | 0.5 | 5.6^ | |
| IR-18 | Neogene deposits | 35.101207 | 58.634732 | 1049 | IR-18.1 | 0.002 | 0.043 | 3.93E−12 | 2.16 | 0.71 | 3.1 | 0.4 | 4.7 | ±2.7 |
| | | | | | IR-18.2 | 0.014 | 0.039 | 1.63E−11 | 5.27 | 0.68 | 7.8 | 0.4 | | |
| | | | | | IR-18.3 | 0.004 | 0.042 | 4.56E−12 | 2.27 | 0.73 | 3.1 | 0.3 | | |
| IR-5 | Pre-Neogene | 35.061950 | 58.369084 | 1067 | IR-5.1 | 0.022 | 0.190 | 3.97E−11 | 4.73 | 0.76 | 6.2 | 0.2 | 16.5 | ±9.8 |
| | | | | | IR-5.2 | 0.195 | 0.198 | 5.07E−10 | 17.09 | 0.66 | 25.9 | 0.5 | | |
| | | | | | IR-5.3 | 0.060 | 0.164 | 1.75E−10 | 14.24 | 0.82 | 17.5 | 0.4 | | |
| IR-17 | Neogene deposits | 35.100512 | 58.673708 | 1014 | IR-17.1 | 0.007 | 0.034 | 1.50E−11 | 7.14 | 0.76 | 9.4 | 0.6 | 7.9 | ±2.1 |
| | | | | | IR-17.2 | 0.007 | 0.054 | 1.24E−11 | 4.71 | 0.73 | 6.4 | 0.3 | | |
| IR-12 | Neogene deposits | 35.104742 | 58.771337 | 1021 | IR-12.1 | 0.003 | 0.032 | 8.51E−13 | 0.56 | 0.58 | 1.0 | 0.7 | 3.1 | ±1.8 |
| | | | | | IR-12.2 | 0.008 | 0.08 | 1.17E−11 | 3.28 | 0.74 | 4.5 | 0.2 | | |
| | | | | | IR-12.3 | 0.060 | 0.07 | 2.71E−11 | 2.81 | 0.74 | 3.8 | 0.2 | | |

*Note:* Amount of helium is given in cubic centimeters in standard temperature and pressure. Amounts of radioactive elements are given in nanograms. Ft—correction factor for alpha-ejection (according to Farley et al., 1996; Hourigan et al., 2005). Uncertainty of the single-grain age is given as 1σ in % (or in Ma), and it includes both the analytical uncertainty and the estimated uncertainty of the Ft. Uncertainty of the sample average age is 1 standard error, as $(SD)/(n)$, where $SD$ = standard deviation of the age replicates, and $n$ = number of age determinations.
*Single age excluded by mean age calculation.

the eastward variation of deformation mechanisms from brittle fracturing to coupled cataclastic flow and dissolution creep during S-C fabric development. This is in agreement with occurrence of hematite-coated fault surfaces systematically observed on the eastern fault strand (Figs. 8C and 8D), which attest to focused fluid flow during fault zone localization, a process that does not occur at shallow (<3 km) crustal depths (Caine et al., 1996; Rowland and Sibson, 2004; Sheldon et al., 2006). Faulting was also intimately associated with regional bulging (anticlinal folding) of the Neogene deposits (Fig. 3), providing further constraints on the Kuh-e-Faghan Fault growth and evolution. Folding is in fact better preserved in the west (cross-sections A-B and C-F in Fig. 3), while it dies out eastward, where it is abruptly interrupted by the eastern fault strand (Fig. 3). It is inferred that folding was caused by the dilatant behavior during initial fracturing of the Neogene deposits. Folding was then amplified by fault zone propagation (fault-related folding, both vertically and along strike) in the Neogene deposits. With increasing shearing, deformation zones matured into discrete through-going fault zones, which localized deformation, preventing further fold amplification.

Such evidence suggests shear deformation occurred under different confining pressure conditions at different locations along the Kuh-e-Faghan Fault, causing a transition from diffuse to localized shear deformation moving eastward along the fault. Differential lithostatic loading between the western and the eastern areas is supported by the stratigraphic and thermochronometric data (see following), which show an overall eastward increase in the Neogene sediment thickness (up to ~4 km) and fault-related exhumation postdating Neogene sedimentation.

Estimation of the fault offset along the Kuh-e-Faghan Fault is hampered by the lack of homologous markers cut by the major fault strands. Nevertheless, an indication of the magnitude of the horizontal separation along the fault strands that make up the Kuh-e-Faghan Fault can be derived from the basement outcrop pattern across the NW-SE–striking trace of the eastern fault strand. The basement block to the north of the eastern fault strand is in fact inferred to have been displaced southeastward from its original position. In this scenario, a horizontal displacement of ~8 km can be proposed (Fig. 3). Further estimates can be obtained from an empirically derived scaling law for faults, relating fault displacement (*D*) to fault length (*L*), fault damage zone (*DT*), and fault core (*CT*) thickness (e.g., Fossen, 2010), respectively. Based on the field observation, the *D-L* diagram provides displacement values ranging from $10^2$ to $10^3$ m, which are in the range of those obtained from the *DT-D* and *CT-D* diagrams. Based on these estimates, it is therefore plausible to assume that the cumulative displacement accumulated along the dextral Kuh-e-Faghan Fault deformation zone would be in the order of a few tens of kilometers.

## Neogene Stratigraphy: Linking Faulting with Sedimentation

The Neogene deposits associated with the Kuh-e-Faghan Fault consist of a fining-upward succession, which is arranged in three main sedimentary cycles. The field observations document a progressive up-section decline in syndepositional tilting, recorded by the gradual disappearance of progressive angular unconformities, coupled with a gradual waning of synsedimentary faulting from Cycle-1 to the base of Cycle-3 (Figs. 5A–5C and 7D). The presence of synsedimentary faulting, together with the overall syndepositional geometry of the Neogene deposits, indicates that their deposition and tilting were controlled by localized uplift along the Kuh-e-Faghan Fault system and suggests fault-related topographic growth during fault system propagation. In such a scenario, the texturally immature and proximally sourced breccias and conglomerates of Cycle-1 are the stratigraphic marker of the growing linear topography associated with Kuh-e-Faghan Fault development. Furthermore, the Neogene deposits show variation in facies distribution and thicknesses along strike of the Kuh-e-Faghan Fault. In particular, the lower portion of Cycle-1, consisting of talus breccias (unit Ng-B), is only present in the western areas (western and central fault strand), with greatest preserved thicknesses documented along the central western fault strand (Fig. 3). This indicates that the fault-related topographic high, from which the breccias were sourced, was initially confined to the western region. The greatest thickness of talus breccias along the western fault strand (Figs. 3 and 5) indicates that the southern side of the Kuh-e-Faghan Fault experienced greater sediment supply influx and/or greater accommodation space. Also the upper unit of Cycle-3 deposits is the thickest (constituting more than half of the total Neogene stratigraphic succession) and the most laterally continuous. Its thickness, lateral stratigraphic continuity, and lack of synsedimentary deformation indicate that it was deposited during a period of tectonic quiescence and most probably of regional subsidence.

Lastly, the Kuh-e-Faghan Fault Neogene stratigraphic succession and the along-strike changes in sedimentary facies, depositional patterns, and thicknesses reflect a history of sedimentary basins strongly influenced by tectonics and regulated by regional and local environmental changes. The eastward increase in the thickness of the Neogene deposits may reflect a migrating depocenter, controlled by the eastward propagation and evolution of the Kuh-e-Faghan Fault during the Neogene.

## Two-Stage Exhumation History

The AHe thermochronometric data set defines two mean age populations, clustering at ca. 18 and ca. 4 Ma. The early Miocene exhumation episode is recorded by basement samples IR-5, IR-8, and IR-15, which are located along the southwestern and central zones of the Kuh-e-Faghan Fault. The early Pliocene exhumation episode is chiefly recorded from the Neogene deposits along the eastern fault strand (Fig. 11).

This early Miocene episode is interpreted as the beginning of faulting, topographic growth, and exhumation along the Kuh-e-Faghan Fault. A source-to-sink scenario is inferred for this time period, when the fault-related topographic growth caused the synchronous erosion/exhumation of the topographically prominent basement units and deposition of the eroded material in the surrounding lowland depocenter. This is supported by (1) the proximal nature of the basal Ng-C conglomerates; (2) the presence of progressively angular unconformities in the basal portion of the Neogene sedimentary successions (Cycle-1 and Cycle-2); and (3) the steepness of bedding, which gradually decreases away from the boundary fault of the fault systems and up section.

The fact that Neogene sediments from the eastern fault strand show AHe ages younger than their source rocks indicates that they have been thermally reset. The reconstructed Neogene stratigraphy indicates that the succession is up to ~4 km thick (Fig. 4), i.e., well above the thickness needed to reset the AHe system at the base of the succession in a normal continental geothermal setting (25–30 °C/km; Chapman, 1986). It is therefore inferred that with the exception of the western and central areas of the Kuh-e-Faghan Fault zone (samples IR-5, IR-8, and IR-15 in Fig. 11), the thickness of these Neogene deposits was sufficient to reset the (U + Th)/He system of the detrital apatite in both the pre-Neogene and the basal Neogene successions. In these areas, a renewed fault activity and fault-related exhumation occurred ca. 4 Ma. This exhumation episode is further documented by the northward and southward postdepositional tilting of the Neogene units, particularly the Ng-GM deposits. This event was characterized by widespread erosion that preferentially targeted the lithologically weaker Cycle-3 marls. In contrast to the first event,

there is no stratigraphic record documenting the topographic growth and general unroofing along the Kuh-e-Faghan Fault. A major erosional unconformity marks the contact between Neogene and Quaternary deposits. Sample IR-18 exhibits an average age that lies between the two mean age clusters. This may reflect partial resetting. Finally, the occurrence of the second exhumation episode along the Kuh-e-Faghan Fault shows that the topmost Neogene successions must be older than 4 Ma. This is compatible with a stratigraphic position equivalent to that of the Upper Red Formation.

The Kuh-e-Faghan Fault experienced a punctuated history of fault-related exhumation. The first fault-related exhumation event started at ca. 18 Ma and progressively waned to a period of relative tectonic quiescence and generalized subsidence during deposition of Cycle-3, sometime before ca. 4 Ma. This time period probably corresponds with the time when synsedimentary faulting and tilting ended (mainly during the deposition of the Cycle-3 Ng-GM deposits). In the absence of any age constraint on the Neogene stratigraphy, the exhumation rate associated with the first exhumation episode cannot be estimated.

The second exhumation event started during the early Pliocene (ca. 4 Ma) and is probably responsible for the present structural architecture of the Kuh-e-Faghan Fault. For each sample that records the early Pliocene event, AHe ages were converted to exhumation rates using a typical continental geothermal gradient of 25 °C/km (e.g., Chapman, 1986), with a long-term averaged annual surface temperature of 16 °C (http://en.climate-data.org/location/5127/) and a closure temperature of 70 °C. Accordingly, the depth of the base of the apatite partial retention zone prior to the onset of denudation must be ~2.1 km. Assuming that the closure isotherms are roughly parallel to local mean elevation and taking into consideration that samples were collected from approximately the same mean elevation at each location, exhumation rates were not adjusted for local sample elevation. The calculated exhumation rates vary between 0.4 and 0.7 km/m.y., with a mean exhumation rate of 0.5 km/m.y. These exhumation rates are comparable with those obtained for the Alborz (0.2–0.7 km/m.y.; Axen et al., 2001; Ballato et al., 2013) and the Zagros (~0.2–0.6 km/m.y.; Mouthereau, 2011) for the same time frame.

## Long-Term Evolution: Fault Nucleation, Propagation, and Growth

Analogue modeling studies have shown that strike-slip fault systems nucleate and evolve from distributed to localized, through-going fault strands (for review, see Dooley and Schreurs, 2012). On the assumption that the topographic evolution and stratigraphic response were structurally controlled during the documented two-stage history of fault zone development, a five-step model is proposed for the long-term evolution of the Kuh-e-Faghan Fault (Fig. 12).

### *Fault System Nucleation*

The fault nucleation stage is attested by the initial topographic growth and basement exhumation in a scenario of diffuse deformation at ca. 18 Ma (Fig. 12A). Topographic growth is inferred to have been achieved by a combination of: (1) transpressive regimes (e.g., Woodcock and Rickards, 2003; Cunningham, 2013), (2) structural irregularities such as stepovers (Aydin and Nur, 1985; Hilley and Arrowsmith, 2008; Finzi et al., 2009; Carne and Little, 2012), (3) local variations in master fault dip (Dair and Cooke, 2009), and (4) pervasive, tectonically induced fracturing and associated volume increase (5%–10%; Braun, 1994; Schopfer and Steyrer, 2001; Le Guerroué and Cobbold, 2006; Schrank and Cruden, 2010). The net result of these processes operating together and over different spatial and temporal scales was the growth of a topographically prominent bulge along the evolving fault zone (Fig. 12A). In the absence of well-developed drainage networks, the eroded material was mainly mobilized by gravity-driven processes and deposited into the adjacent basins as thick packages of proximally sourced breccias at the base of the Neogene Cycle-1 (Ng-B and Ng-C).

### *Fault Localization and Propagation*

Faulting was probably initially accommodated by a network of distributed en-echelon Riedel shears that successively merged by sideways propagation or linkage to form through-going master faults (Fig. 12B). In this context, due to the strain hardening and velocity-strengthening properties of poorly consolidated syntectonic sediments (e.g., Scholz, 2002), fault propagation was probably inhibited within the newly deposited material. This had the effect of favoring faulting along areas free of unconsolidated sediments, causing faulting activity to migrate inward, gradually localizing along subvertical fault zones at the basement-sediment interface (Le Guerroué and Cobbold, 2006; Fig. 12B). The positive feedbacks among topographic growth, erosion, sedimentation, and inward fault migration are the primary driver for the progressive narrowing of the fault system and the associated topographic growth. As a result, synsedimentary faulting accompanied the topographic growth and the progressive tilting of the deposits. The drainage network developed further as deformation continued, creating larger catchments capable of producing yet more texturally mature sediments. Such conditions produced proximal alluvial fan deposits consisting of gravelly sandstones, intermediate alluvial plains consisting of clinostratified and cross-bedded channel fill and bar sandstone deposits, which distally evolved into fluvio-palustrine facies (Neogene Cycle-2 deposits). Distribution of the Cycle-2 deposits indicates increasing thicknesses toward the NE, suggesting preferred sediment influx/rooting toward this region (Fig. 12B).

### *Fault Termination*

Development of trailing extensional imbricate fan terminations at the eastern fault tips (Woodcock and Fischer, 1986; Figs. 3 and 12C) attests to strike-slip shear dissipation at fault zone terminations. The extensional/transtensional faulting and the associated fault-controlled depocenters (cf. Wu et al., 2009) developed at the same time as deposition of the basal part of the Neogene Cycle-3 (Ng-GM deposits). Their distribution and the syntectonic character of deposition allow us to define the distribution and geometries of the subsiding areas and basin boundary faults (Fig. 12C).

### *Tectonic Quiescence*

Tectonic activity progressively waned during the deposition of unit Ng-GM, as attested by the gradual up-section disappearance of synsedimentary faulting and tilting. The Cycle-3 Ng-MS deposits progressively covered the entire Kuh-e-Faghan Fault area. Their thickness, lateral stratigraphic continuity, and lack of synsedimentary deformation indicate that they were deposited during a period of tectonic quiescence and, most probably, of regional subsidence (Fig. 12D).

### *Renewed Faulting*

Deformation and faulting activity resumed at ca. 4 Ma, reactivating most of the preexisting faults strands and creating new ones that propagated further eastward (Fig. 12E). This renewed fault activity is considered to be responsible for the current fault zone geometry, developed in a regime of simple shear–dominated strike-slip faulting. It affected a heterogeneous upper-crustal section, due to the anisotropic distribution of the Neogene deposits. To the east, where higher confining pressure was provided by the thick Neogene sediments (up to 4 km in thickness), combined cataclastic flow and dissolution creep allowed mature fault zones to develop. To the west, the reduced confining pressure means the fault zone was less localized and characterized by dilatant brittle behavior of the Neogene deposits, associated with volume

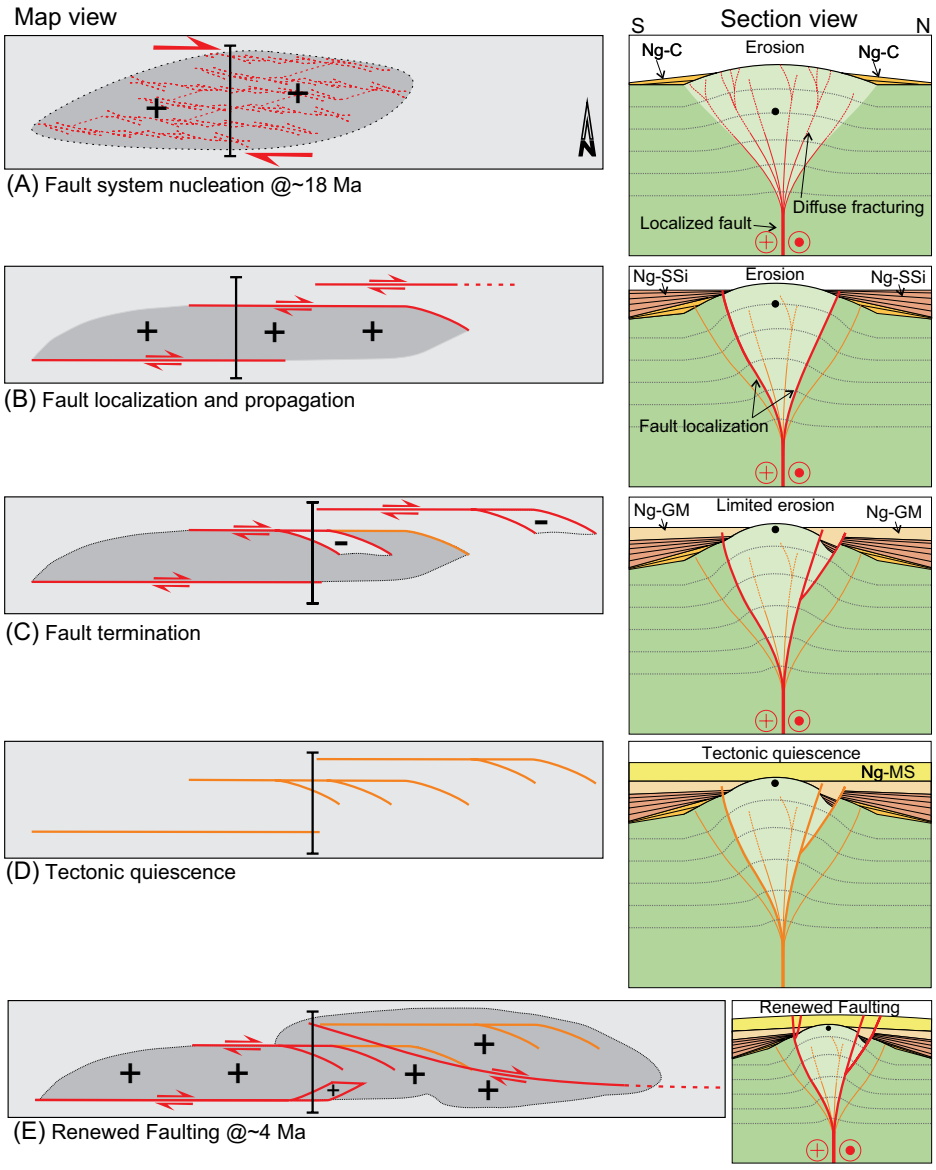


**Figure 12. Conceptual spatio-temporal model for the long-term evolution of the Kuh-e-Faghan dextral fault system (see text for further details). Key to the figure: dark-gray areas with plus (+)—uplift; light-gray areas with minus (–)—subsidence; red—active fault; orange—inactive fault. The black dot indicates the hypothetical exhumation path followed by the basement rocks during the punctuated tectonic activity of the Kuh-e-Faghan Fault. For lithological symbols, refer to Figure 3.**

increase accommodated by the regional anticlinal folding of the Neogene deposits (Fig. 3). In the western area, topographic growth was also achieved by the left-stepping geometry between the dextral western fault strand and the central fault strand (Fig. 3). The eastward propagation of the Kuh-e-Faghan Fault system prevented further fold amplification, with a progressive localization of strain under higher confining pressure conditions.

The renewed topographic growth along the Kuh-e-Faghan Fault was accompanied by widespread erosion and unroofing (Fig. 12E). The fact that no syntectonic deposits are preserved in proximity (tens of kilometers) to the Kuh-e-Faghan Fault during this second event suggests that it was accompanied by an erosional phase, as also testified by a regional pediment cutting the tilted Neogene deposits, during which time the eroded material was efficiently transported away from the Kuh-e-Faghan Fault area.

During the late Pleistocene and Holocene, new, climate-driven, aggradation phases took place, as testified by the different generations of alluvial fans and fluvial terraces widely recognized in eastern Iran (Regard et al., 2006; Fattahi et al., 2007; Walker and Fattahi, 2011; Foroutan et al., 2014). Evidence of dextral transpressional shear affecting these Quaternary alluvial deposits along the Kuh-e-Faghan Fault system suggests that the transpressional regime renewed and is probably still active along the Kuh-e-Faghan Fault, being responsible for the present topography of the Kuh-e-Faghan Fault deformation zone.

From this scenario, assuming that renewed faulting started at ca. 4 Ma and continued at a constant rate, estimates of the slip rates based on the estimated horizontal apparent displacement (~8 km) along the Kuh-e-Faghan Fault strands (eastern fault strand) are in the range of ~2 mm/yr. The calculated slip rate is comparable with those obtained for the E-W–oriented strike-slip Doruneh fault, ranging from 1.3 to 2.5 mm/yr (Fattahi et al., 2007; Farbod et al., 2011; Walpersdorf et al., 2014), and Dasht-e-Bayaz fault, ranging from 1 to 2.5 mm/yr (Berberian and Yeats, 1999; Walker et al., 2004).

## Regional Implications

The early Miocene tectonic/exhumation event recognized along the Kuh-e-Faghan Fault is in good agreement with the regional thermochronometric results, as obtained from the Zagros, Alborz, and Talesh areas (Khadivi et al., 2012; Ballato et al., 2013; Madanipour et al., 2013). It also correlates with the late-stage, early Miocene exhumation of the Kashmar-Kerman tectonic zone (Fig. 1), which is interpreted as the transition from extensional to compressional tectonics in the region (Verdel et al., 2007). Within this context, the reconstructed source-to-sink scenario along the Kuh-e-Faghan Fault places onset of deposition of Neogene continental successions of the Upper Red Formation in central Iran at the early Miocene. This age is compatible with the Burdigalian–Messinian age of the Upper Red Formation (Ballato et al., 2008), but it contrasts with the recently proposed Burdigalian–Serravallian age for the "e" member of the Qom Formation (Hadavi et al., 2010), which instead implies a possible post-Serravallian onset of the continental deposition of the Upper Red Formation. This suggests a diachronic distribution of the Neogene continental deposits with a control operated by the regional tectonics on the Neogene sedimentary facies distribution and stratigraphy in central Iran.

The early Pliocene event was coeval with a regional tectonic reorganization, as inferred from the recognized acceleration in uplift rates in the Alborz and Talesh Mountains and by

fault kinematic changes in the Kopeh Dagh and along the Zagros-Makran transfer zone (Axen et al., 2001; Regard et al., 2005; Shabanian et al., 2009a; Hollingsworth et al., 2010; Rezaeian et al., 2012; Madanipour et al., 2013; Robert et al., 2014). The Miocene–Pliocene boundary also corresponds to the time when the Zagros collisional zone became overthickened to sustain further shortening (Allen et al., 2004; Austermann and Iaffaldano, 2013).

The cause of the Pliocene regional tectonic event across the Iranian Plateau is still uncertain, with several geodynamic/tectonic scenarios proposed so far: (1) onset of subduction in the South Caspian Basin (Jackson et al., 2002; Mouthereau et al., 2012; Madanipour et al., 2013); (2) a switch from westward/northwestward to northeastward escape of central Iran, triggered by the Afghan and western margin of the Indian collision, sealing off a free face at the eastern side of the Arabia-Eurasia collision zone (Allen et al., 2011); and (3) activation of the Zagros-Makran transfer zone between the collision domain and the Makran subduction domain (eastern Iran; Regard et al., 2010).

Regardless of the ultimate cause of the Pliocene event, our AHe age data constitute the first direct documentation of such an event in central Iran. Therefore, a reappraisal of the Neogene–Quaternary space-time kinematic evolution and fault distribution within central Iran is needed. In particular, the following evidence is not compatible with the kinematic configuration and rigid block rotation model proposed for central Iran: (1) fault zone (re)activation and kinematic shifts punctuated in time and space at the northern edge of the Lut block during Neogene–Quaternary (Javadi et al., 2013; Nozaem et al., 2013; this study); and (2) Neogene–Quaternary NW-SE to E-W dextral strike-slip kinematics acting at rates compatible with the regional average values along the northern edge of the Lut block to the south of the Doruneh fault (cf. Allen et al., 2004, 2011; Walker and Jackson, 2004; Mattei et al., 2012; Walpersdorf et al., 2014).

We tentatively propose that the Neogene–Quaternary deformation in the Iranian Plateau has been primarily controlled by spatial and temporal variations in the degree of tectonic coupling along the Arabia-Eurasia collision interface, in the framework of a constant N-S–directed convergence velocity scenario (McQuarrie and van Hinsbergen, 2013). Indeed, the along-strike variation from continent-continent convergence in the Zagros to ocean-continent convergence in the Makran and, hence, from a fully to partially coupled collisional boundary (Fig. 1), might have imposed a northeastward escape component to the intraplate domain (Regard et al., 2010) with polycyclic reactivation of the Kashmar-Kerman tectonic zone along the Kuh-e-Sarhangi, Kuh-e-Faghan, and Doruneh fault strands (Verdel et al., 2007; Javadi et al., 2013; Nozaem et al., 2013; this study). In this scenario, the N-S dextral strike-slip faults at the edges of the Central East Iran microcontinent may have accommodated the differential displacement between the collision domain of central Iran and the Makran subduction domain of eastern Iran. This has been occurring between nonrotating blocks such as between central and eastern Iran (Deshir and Anar faults; Fig. 1; Meyer and Le Dortz, 2007).

### Implications for Topographic Growth along Intraplate Strike-Slip Faults

Integration of the multidisciplinary data set presented in this study results in a model for long-term, spatially and temporally punctuated fault system evolution. Based on the regional scenario and synchronicity with the regional deformation events leading to the growth of the Iranian Plateau, the reason for the nonlinear temporal evolution of intraplate faulting is partially attributable to changes in the regional (far-field) stress regime through time. Tectonic stresses are generated at the plate margins and are transferred to the intraplate domains, where they interact with preexisting structures and local (near-field) kinematically induced stress regimes.

Several other factors influence deformation in the near-field at the scale of the developing fault system, such as spatial changes in the degree of fault development maturity and structural complexity during fault development. The spatial-temporal changes in those interactions and feedbacks regulate the way plate-boundary stresses are transferred to the intraplate domains and may ultimately be responsible for the punctuated development of intraplate deformation and associated topographic growth. In particular, the study recognizes that the positive feedbacks among topographic growth, erosion, sedimentation, and inward fault migration are the primary drivers for the progressive fault zone localization, narrowing of the fault system, and its topographic growth.

## CONCLUSIONS

The main results of this study are as follows:

(1) The Kuh-e-Faghan Fault consists of a major E-W–striking, 80-km-long dextral strike-slip brittle deformation zone, made up of three broadly left-stepping, E-W–striking, dextral, strike-slip fault strands, which cut through the Neogene sedimentary cover and the unconformably overlying Quaternary deposits.

(2) The Kuh-e-Faghan Fault is characterized by simple shear–dominated dextral strike-slip deformation. The along-strike spatial variations of the fault orientations, kinematics, and strain regimes (restraining and releasing areas) reflect the different ways by which the overall E-W right-lateral shear is accommodated, distributed, and partitioned along the principal and minor fault strands of the Kuh-e-Faghan Fault system.

(3) AHe thermochronometry indicates that the Kuh-e-Faghan Fault system propagation was punctuated in time and space and associated with two major episodes of fault-related exhumation, at ca. 18 Ma (early Miocene) and ca. 4 Ma (early Pliocene).

(4) The stratigraphic, structural, and thermochronometric data sets show that the Kuh-e-Faghan Fault nucleated in the west and propagated eastward in two punctuated events.

(5) The first faulting/exhumation episode is chiefly recorded by the structure and deposition of the Neogene deposits along the Kuh-e-Faghan Fault, where a source-to-sink scenario can be reconstructed for this time frame, when topographic growth caused the synchronous erosion/exhumation of the pre-Neogene units and deposition of the eroded material in the surrounding fault-bounded continental depocenters.

(6) The Kuh-e-Faghan Fault gradually entered a period of relative tectonic quiescence and, probably, regional subsidence, during which a thick pile of fine-grained onlapping sediments was deposited, and this caused the resetting of the (U + Th)/He system of the detrital apatite grains hosted both within the pre-Neogene and the basal Neogene successions. The second faulting episode at ca. 4 Ma, recorded by the AHe ages and by the further tilting of the Neogene deposits, caused the final exhumation of the fault system, resulting in the current fault zone geometry and topography.

(7) The two fault-related exhumation events are nearly coincident with (a) the well-documented acceleration of collision-related uplift in the early Miocene along the Arabia-Eurasia collision zone, and (b) the inferred early Pliocene tectonic reorganization of central Iran.

Results from this study suggest that the intraplate deformation zones are particularly sensitive to major tectonic changes occurring at the plate boundaries (far-field effects), and, as such, they can be regarded as a gauge for plate-tectonics–induced state-of-stress changes at the plate boundaries. The results also suggest that the propagation and evolution of intraplate strike-slip fault systems are accompanied by substantial topographic growth, exhumation, erosion, and production of syntectonic deposits, the distribution, geometry and facies characteristics of which are strongly influenced by the spatio-temporal propagation history and structural evolution of the fault system (near-field effects).

## APPENDIX: (U-Th)/He THERMOCHRONOMETRY

(U-Th)/He thermochronometry is based on the ingrowth of a particle's [He], produced mainly by U and Th decay. The He diffusivity within the crystal lattice is a function primarily of temperature and in minor ways of grains size and distribution of parent isotope (Ehlers and Farley, 2003). Helium diffusive loss is complete in typical apatites at temperatures in excess of ~75 °C; it becomes limited between ~75 °C and ~40 °C, an interval called the partial retention zone (HePRZ; House et al , 1999; Farley, 2000). Assuming no other source for the He, the measured He age records the time the rock cooled below the closure temperature of ~70 °C.

Inclusion-free apatites for (U-Th)/He analysis were handpicked under a high-magnification binocular microscope with cross-polarized light. Single crystals were packed into Pt foil capsules. In total, 3–5 apatite grains were analyzed for each sample. Helium was extracted by heating the Pt-tubes at 600–700 °C for 1–2 min using a laser diode following the procedures described by Foeken et al. (2006). The $^{4}$He concentrations were measured by comparison to a calibrated standard $^{4}$He using a Hiden HAL3F quadrupole mass spectrometer equipped with an electron multiplier. The accuracy of measurements was checked by repeated measurements of an in-house He standard. System blank levels were trivial in comparison to measured He abundances, and no correction was necessary. Apatites were then dissolved in 5% $HNO_3$ with $^{235}$U and $^{230}$Th spikes and measured by VG Plasma Quad 2 inductively coupled plasma–mass spectrometer. Correction for He recoil loss (Ft) was made using conventional procedures (Farley et al., 1996).


### ACKNOWLEDGMENTS

Special thanks go to M.R. Mazinani for assistance during field work. The manager and staff of Khanyeh-e-Moallem of Kashmar are warmly thanked for their kind hospitality. We also thank Ali Rastpour and Hassan Faraji for driving to the field and logistic support. F. Salvini is thanked for his advice during fault population analysis. Constructive reviews by F. Mouthreau and D. Peacock significantly contributed to improve the final version of the manuscript. This project has been funded by TOPOMOD Marie Curie ITN project (grant agreement 264517).


### REFERENCES CITED


Agard, P., Omrani, J., Jolivet, L., Whitechurch, H., Vrielynck, B., Spakman, W., Monié, P., Meyer, B., and Wortel, R., 2011, Zagros orogeny: A subduction-dominated process: Geological Magazine, v. 148, p. 692–725, doi:10.1017/S0016756811000046X.

Aghanabati, A., 2004, Geology of Iran: Teheran, Geological Survey of Iran, 582 p.

Aitken, A.R.A., Raimondo, T., and Capitanio, F.A., 2013, The intraplate character of supercontinent tectonics: Gondwana Research, v. 24, p. 807–814, doi:10.1016/j.gr.2013.03.005.

Allen, M., Jackson, J., and Walker, R., 2004, Late Cenozoic reorganization of the Arabia-Eurasia collision and the comparison of short-term and long-term deformation rates: Tectonics, v. 23, TC2008, doi:10.1029/2003tc001530.

Allen, M.B., and Armstrong, H.A., 2008, Arabia-Eurasia collision and the forcing of mid-Cenozoic global cooling: Palaeogeography, Palaeoclimatology, Palaeoecology, v. 265, p. 52–58, doi:10.1016/j.palaeo.2008.04.021.

Allen, M.B., Kheirkhah, M., Emami, M.H., and Jones, S.J., 2011, Right-lateral shear across Iran and kinematic change in the Arabia-Eurasia collision zone: Geophysical Journal International, v. 184, no. 2, p. 555–574, doi:10.1111/j.1365-246X.2010.04874.x.

Amini, A., 1997, Provenance and Depositional Environment of the Upper Red Formation, Central Zone Iran [Ph.D. thesis]: Manchester, UK, University of Manchester, 320 p.

Austermann, J., and Iaffaldano, G., 2013, The role of the Zagros orogeny in slowing down Arabia-Eurasia convergence since ~5 Ma: Tectonics, v. 32, p. 351–363, doi:10.1002/tect.20027.

Avouac, J.-P., Ayoub, F., Wei, S., Ampuero, J.-P., Meng, L., Leprince, S., Jolivet, R., Duputel, Z., and Helmberger, D., 2014, The 2013, Mw 7.7 Balochistan earthquake, energetic strike-slip reactivation of a thrust fault: Earth and Planetary Science Letters, v. 391, p. 128–134, doi:10.1016/j.epsl.2014.01.036.

Axen, G.J., Lam, P.S., Grove, M., Stockli, D.F., and Hassanzadeh, J., 2001, Exhumation of the west-central Alborz Mountains, Iran, Caspian subsidence, and collision-related tectonics: Geology, v. 29, p. 559–562, doi:10.1130/0091-7613(2001)029<0559:EOTWCA>2.0.CO;2.

Aydin, A., and Nur, A., 1985, The types and role of stepovers in strike-slip tectonics, *in* Biddle, K.T., and Christie-Blick, N., eds., Strike-Slip Deformation, Basin Formation, and Sedimentation: Society of Economic Paleontologists and Mineralogists Special Publication 37, p. 35–45.

Ballato, P., Nowaczyk, N.R., Landgraf, A., Strecker, M.R., Friedrich, A., and Tabatabaei, S.H., 2008, Tectonic control on sedimentary facies pattern and sediment accumulation rates in the Miocene foreland basin of the southern Alborz Mountains, northern Iran: Tectonics, v. 27, TC6001, doi:10.1029/2008TC002278.

Ballato, P., Uba, C.E., Landgraf, A., Strecker, M.R., Sudo, M., Stockli, D.F., Friedrich, A., and Tabatabaei, S.H., 2011, Arabia-Eurasia continental collision: Insights from late Tertiary foreland-basin evolution in the Alborz Mountains, northern Iran: Geological Society of America Bulletin, v. 123, p. 106–131, doi:10.1130/B30091.1.

Ballato, P., Stockli, D.F., Ghassemi, M.R., Landgraf, A., Strecker, M.R., Hassanzadeh, J., Friedrich, A., and Tabatabaei, S.H., 2013, Accommodation of transpressional strain in the Arabia-Eurasia collision zone: New constraints from (U-Th)/He thermochronology in the Alborz Mountains, north Iran: Tectonics, v. 32, p. 1–18, doi:10.1029/2012TC003159.

Bayasgalan, A., Jackson, J., Ritz, J.-F., and Carretier, S., 1999, 'Forebergs,' flower structures, and the development of large intra-continental strike-slip faults: The Gurvan Bogd fault system in Mongolia: Journal of Structural Geology, v. 21, p. 1285–1302, doi:10.1016/S0191-8141(99)00064-4.

Behroozi, A., Sahbaei, M., Etemadi, N., Zedeh, A. A., Ghomashi, A., and Moghtader, M., 1987, Geological map of Feyz Abad: Teheran, Geological Survey of Iran, scale 1:100,000.

Berberian, M., 1974, A brief geological description of north-central Iran, *in* Tchalenko J.S., Ambraseys, N N., Berberian, M., Iranmanesh, M.H., Mohajer-Ashjai, A., Bailly, M., and Arsovsky, M., eds., Materials for the Study of the Seismotectonics of Iran, North-Central Iran: Geological Survey of Iran Report 29, p. 127–138.

Berberian, M., 2014, Earthquakes and Coseismic Surface Faulting on the Iranian Plateau: Oxford, Elsevier Science, 776 p.

Berberian, M., and King, G.C.P., 1981, Towards a paleogeography and tectonic evolution of Iran: Canadian Journal of Earth Sciences, v. 18, no. 2, p. 210–265, doi:10.1139/e81-019.

Berberian, M., and Yeats, R.S., 1999, Patterns of historical earthquake rupture in the Iranian Plateau: Bulletin of the Seismological Society of America, v. 89, no. 1, p. 120–139.

Braun, J., 1994, Three-dimensional numerical simulations of crustal-scale wrenching using a non-linear failure criterion: Journal of Structural Geology, v. 16, no. 8, p. 1173–1186, doi:10.1016/0191-8141(94)90060-4.

Buscher, J.T., and Spotila, J.A., 2007, Near-field response to transpression along the southern San Andreas fault, based on exhumation of the northern San Gabriel Mountains, southern California: Tectonics, v. 26, no. 5, TC5004, doi:10.1029/2006TC002017.

Caine, J.S., Evans, J.P., and Forster, C.B., 1996, Fault zone architecture and permeability structure: Geology, v. 24, no. 11, p. 1025–1028, doi:10.1130/0091-7613(1996)024<1025:FZAAPS>2.3.CO;2.

Calais, E., Vergnolle, M., San'kov, V., Lukhnev, A., Miroshnitchenko, A., Amarjargal, S., and Déverchère, J., 2003, GPS measurements of crustal deformation in the Baikal-Mongolia area (1994–2002): Implications for current kinematics of Asia: Journal of Geophysical Research–Solid Earth, v. 108, no. B10, 2501, doi:10.1029/2002JB002373.

Carne, R.C., and Little, T.A., 2012, Geometry and scale of fault segmentation and deformational bulging along an active oblique-slip fault (Wairarapa fault, New Zealand): Geological Society of America Bulletin, v. 124, no. 7–8, p. 1365–1381, doi:10.1130/B30535.1.

Chapman, D.S., 1986, Thermal gradients in the continental crust, *in* Dawson, J.B., Carswell, D.A., Hall, J., and Wedepohl, K.H., eds., The Nature of the Lower Continental Crust: Geological Society of London Special Publication 24, no. 1, p. 63–70, doi:10.1144/GSL.SP.1986.024.01.07.

Christie-Blick, N., and Biddle, K.T., 1985, Deformation and basin formation along strike-slip faults, *in* Biddle, K.T., and Christie-Blick, N., eds., Strike-Slip Deformation, Basin Formation, and Sedimentation: The Society of Economic Paleontologists and Mineralogist Special Publication 37, p. 1–34.

Cloetingh, S., Ziegler, P.A., Beekman, F., Andriessen, P.A.M., Matenco, L., Bada, G., Garcia-Castellanos, D., Hardebol, N., Dèzes, P., and Sokoutis, D., 2005, Lithospheric memory, state of stress and rheology: Neotectonic controls on Europe's intraplate continental topography: Quaternary Science Reviews, v. 24, no. 3–4, p. 241–304, doi:10.1016/j.quascirev.2004.06.015.

Cox, S.C., Stirling, M.W., Herman, F., Gerstenberger, M., and Ristau, J., 2012, Potentially active faults in the rapidly eroding landscape adjacent to the Alpine fault, central Southern Alps, New Zealand: Tectonics, v. 31, no. 2, TC2011, doi:10.1029/2011TC003038.

Cunningham, D., 2013, Mountain building processes in intracontinental oblique deformation belts: Lessons from the Gobi Corridor, Central Asia: Journal of Structural Geology, v. 46, p. 255–282, doi:10.1016/j.jsg.2012.08.010.

Cunningham, W.D., and Mann, P., 2007, Tectonics of strike-slip restraining and releasing bends, *in* Cunningham, W.D., and Mann, P., eds., Tectonics of Strike-Slip Restraining and Releasing Bends: Geological Society of London Special Publication 290, p. 1–12, doi:10.1144/SP290.1.

Dair, L., and Cooke, M.L., 2009, San Andreas fault geometry through the San Gorgonio Pass, California: Geology, v. 37, no. 2, p. 119–122, doi:10.1130/G25101A.1.

Daneshian, J., and Dana, L.R., 2007, Early Miocene benthic foraminifera and biostratigraphy of the Qom Formation, Deh Namak, central Iran: Journal of Asian Earth Sciences, v. 29, no. 5–6, p. 844–858, doi:10.1016/j.jseaes.2006.06.003.

Di Vincenzo, G., Rossetti, F., Viti, C., and Balsamo, F., 2013, Constraining the timing of fault reactivation: Eocene coseismic slip along a Late Ordovician ductile shear zone (northern Victoria Land, Antarctica): Geological Society of America Bulletin, v. 125, no. 3–4, p. 609–624, doi:10.1130/B30670.1.

Doblas, M., 1998, Slickenside kinematic indicators: Tectonophysics, v. 295, no. 1–2, p. 187–197, doi:10.1016/S0040-1951(98)00120-6.

Dooley, T.P., and Schreurs, G., 2012, Analogue modelling of intraplate strike-slip tectonics: A review and new experimental results: Tectonophysics, v. 574–575, p. 1–71, doi:10.1016/j.tecto.2012.05.030.

Dyksterhuis, S., and Müller, R.D., 2008, Cause and evolution of intraplate orogeny in Australia: Geology, v. 36, no. 6, p. 495–498, doi:10.1130/G24536A.1.

Eftekhar-Nezhad, J., Aghanabati, A., Hamzehpour, B., and Baroyant, V., 1976, Geological map of Kashmar: Teheran, Geological Survey of Iran, scale 1:250,000.

Ehlers, T.A., and Farley, K.A., 2003, Apatite (U-Th)/He thermochronometry: Methods and applications to problems in tectonic and surface processes: Earth and Planetary Science Letters, v. 206, p. 1–14, doi:10.1016/S0012-821X(02)01069-5.

Ellis, S., 1996, Forces driving continental collision: Reconciling indentation and mantle subduction tectonics: Geology, v. 24, no. 8, p. 699–702, doi:10.1130/0091-7613(1996)024<0699:FDCCRI>2.3.CO;2.

Farbod, Y., Bellier, O., Shabanian, E., and Abbassi, M.R., 2011, Geomorphic and structural variations along the Doruneh fault system (central Iran): Tectonics, v. 30, no. 6, TC6014, doi:10.1029/2011TC002889.

Farley, K.A., 2000, Helium diffusion from apatite: General behavior as illustrated by Durango fluorapatite: Journal of Geophysical Research–Solid Earth, v. 105, no. B2, p. 2903–2914, doi:10.1029/1999JB900348.

Farley, K.A., Wolf, R.A., and Silver, L.T., 1996, The effects of long alpha-stopping distances on (U-Th)/He ages: Geochimica et Cosmochimica Acta, v. 60, no. 21, p. 4223–4229, doi:10.1016/S0016-7037(96)00193-7.

Fattahi, M., Walker, R.T., Khatib, M.M., Dolati, A., and Bahroudi, A., 2007, Slip-rate estimate and past earthquakes on the Doruneh fault, eastern Iran: Geophysical Journal International, v. 168, no. 2, p. 691–709, doi:10.1111/j.1365-246X.2006.03248.x.

Finzi, Y., Hearn, E., Ben-Zion, Y., and Lyakhovsky, V., 2009, Structural properties and deformation patterns of evolving strike-slip faults: Numerical simulations incorporating damage rheology: Pure and Applied Geophysics, v. 166, no. 10–11, p. 1537–1573, doi:10.1007/s00024-009-0522-1.

Fitzgerald, P.G., Stump, E., and Redfield, T.F., 1993, Late Cenozoic uplift of Denali and its relation to relative plate motion and fault morphology: Science, v. 259, p. 497–499, doi:10.1126/science.259.5094.497.

Fitzgerald, P.G., Sorkhabi, R.B., Redfield, T.F., and Stump, E., 1995, Uplift and denudation of the central Alaska Range: A case study in the use of apatite fission track thermochronology to determine absolute uplift parameters: Journal of Geophysical Research–Solid Earth, v. 100, p. 20,175–20,191, doi:10.1029/95JB02150.

Foeken, J.P.T., Stuart, F.M., Dobson, K.J., Persano, C., and Vilbert, D., 2006, A diode laser system for heating minerals for (U-Th)/He chronometry: Geochemistry Geophysics Geosystems, v. 7, no. 4, Q04015, doi:10.1029/2005GC001190.

Foeken, J.P.T., Persano, C., Stuart, F.M., and ter Voorde, M., 2007, Role of topography in isotherm perturbation: Apatite (U-Th)/He and fission track results from the Malta tunnel, Tauern Window, Austria: Tectonics, v. 26, no. 3, TC3006, doi:10.1029/2006TC002049.

Foroutan, M., Meyer, B., Sébrier, M., Nazari, H., Murray, A.S., Le Dortz, K., Shokri, M.A., Arnold, M., Aumaître, G., Bourlès, D., Keddadouche, K., Solaymani Azad, S., and Bolourchi, M.J., 2014, Late Pleistocene–Holocene right slip rate and paleoseismology of the Nayband fault, western margin of the Lut block, Iran: Journal of Geophysical Research–Solid Earth, v. 119, no. 4, p. 3517–3560, doi:10.1002/2013JB010746.

Fossen, H., 2010, Structural Geology: Cambridge, UK, Cambridge University Press, 480 p.

Fossen, H., Tikoff, B., and Teyssier, C., 1994, Strain modeling of transpressional and transtensional deformation: Norsk Geologisk Tidsskrift, v. 74, no. 3, p. 134–145.

Gavillot, Y., Axen, G.J., Stockli, D.F., Horton, B.K., and Fakhari, M.D., 2010, Timing of thrust activity in the High Zagros fold-thrust belt, Iran, from (U-Th)/He thermochronometry: Tectonics, v. 29, no. 4, TC4025, doi:10.1029/2009TC002484.

Ghomashi, A., Masoomi, R., Hosseiny, S.Z., Taheri, J., Shamanian, G., Kaveh, N.S., Baheremand, M., and Razavi, M.A., 2001, Geological map of Kashmar: Teheran, Geological Survey of Iran, scale 1:100,000.

Granier, T., 1985, Origin, damping, and pattern of development of faults in granite: Tectonics, v. 4, no. 7, p. 721–737, doi:10.1029/TC004i007p00721.

Guest, B., Stockli, D.F., Grove, M., Axen, G.J., Lam, P.S., and Hassanzadeh, J., 2006, Thermal histories from the central Alborz Mountains, northern Iran: Implications for the spatial and temporal distribution of deformation in northern Iran: Geological Society of America Bulletin, v. 118, no. 11–12, p. 1507–1521, doi:10.1130/b25819.1.

Hadavi, F., Notghi Moghaddam, M., and Mousazadeh, H., 2010, Burdigalian–Serravallian calcareous nannoplanktons from Qom Formation, north-center Iran: Arabian Journal of Geosciences (Prague), v. 3, no. 2, p. 133–139, doi:10.1007/s12517-009-0052-2.

Hafkenscheid, E., Wortel, M.J.R., and Spakman, W., 2006, Subduction history of the Tethyan region derived from seismic tomography and tectonic reconstructions: Journal of Geophysical Research–Solid Earth, v. 111, B08401, doi:10.1029/2005jb003791.

Hassami, K., Jamali, F., and Tabassi, H., 2003, Major active faults of Iran: Tehran, Iran, International Institute of Earthquake Engineering and Seismology, scale 1:2,500,000.

Hatzfeld, D., and Molnar, P., 2010, Comparisons of the kinematics and deep structures of the Zagros and Himalaya and of the Iranian and Tibetan Plateaus and geodynamic implications: Reviews of Geophysics, v. 48, no. 2, RG2005, doi:10.1029/2009RG000304.

Headley, R.M., Enkelmann, E., and Hallet, B., 2013, Examination of the interplay between glacial processes and exhumation in the Saint Elias Mountains, Alaska: Geosphere, v. 9, no. 2, p. 229–241, doi:10.1130/GES00810.1.

Heidbach, O., Tingay, M., Barth, A., Reinecker, J., Kurfeß, D., and Müller, B., The World Stress Map database release 2008, doi:10.1594/GFZ.WSM.Rel2008.

Hessami, K., Koyi, H.A., Talbot, C.J., Tabasi, H., and Shabanian, E., 2001, Progressive unconformities within an evolving foreland fold-thrust belt, Zagros Mountains: Journal of the Geological Society of London, v. 158, no. 6, p. 969–981, doi:10.1144/0016-764901-007.

Hilley, G.E., and Arrowsmith, J.R., 2008, Geomorphic response to uplift along the Dragon's Back pressure ridge, Carrizo Plain, California: Geology, v. 36, no. 5, p. 367–370, doi:10.1130/G24517A.1.

Holdsworth, R.E., Handa, M., Miller, J.A., and Buick, I.S., 2001, Continental reactivation and reworking: An introduction, *in* Miller, J.A., Holdsworth, R.E., Buick, I.S., and Hand, M., eds., Continental Reactivation and Reworking: Geological Society of London Special Publication 184, p. 1–12, doi:10.1144/GSL.SP.2001.184.01.01.

Hollingsworth, J., Fattahi, M., Walker, R., Talebian, M., Bahroudi, A., Bolourchi, M.J., Jackson, J., and Copley, A., 2010, Oroclinal bending, distributed thrust and strike-slip faulting, and the accommodation of Arabia-Eurasia convergence in NE Iran since the Oligocene: Geophysical Journal International, v. 181, no. 3, p. 1214–1246, doi:10.1111/j.1365-246X.2010.04591.x.

Homke, S., Vergés, J., Serra-Kiel, J., Bernaola, G., Sharp, I., Garcés, M., Montero-Verdú, I., Karpuz, R., and Goodarzi, M.H., 2009, Late Cretaceous–Paleocene formation of the proto–Zagros foreland basin, Lurestan Province, SW Iran: Geological Society of America Bulletin, v. 121, no. 7–8, p. 963–978, doi:10.1130/B26035.1.

Homke, S., Vergés, J., Van Der Beek, P., Fernàndez, M., Saura, E., Barbero, L., Badics, B., and Labrin, E., 2010, Insights in the exhumation history of the NW Zagros from bedrock and detrital apatite fission-track analysis: Evidence for a long-lived orogeny: Basin Research, v. 22, no. 5, p. 659–680, doi:10.1111/j.1365-2117.2009.00431.x.

Hourigan, J.K., Reiners, P.W., and Brandon, M.T., 2005, U-Th zonation-dependent alpha-ejection in (U-Th)/He chronometry: Geochimica et Cosmochimica Acta, v. 69, no. 13, p. 3349–3365.

House, M.A., Farley, K.A., and Kohn, B.C., 1999, An empirical test of helium diffusion in apatite: Borehole data from the Otway Basin, Australia: Earth and Planetary Science Letters, v. 170, p. 463–474, doi:10.1016/S0012-821X(99)00120-X.

Jackson, J., and McKenzie, D., 1984, Active tectonics of the Alpine-Himalayan Belt between western Turkey and Pakistan: Geophysical Journal International, v. 77, no. 1, p. 185–264, doi:10.1111/j.1365-246X.1984.tb01931.x.

Jackson, J., Priestley, K., Allen, M., and Berberian, M., 2002, Active tectonics of the South Caspian Basin: Geophysical Journal International, v. 148, no. 2, p. 214–245, doi:10.1046/j.1365-246X.2002.01588.x.

Jalilian, M., Etemadi, N., Zadeh, A.A., Manouchehri, M., Pour, M.J.V., Tehrani, N.A., Behrouzi, A., Kholghi, M.H., and Naini, M.A., 1992, Geological map of Torbat-e-Heydarieh: Tehran, Iran, Geological Survey of Iran, scale 1:250,000.

Javadi, H.R., Ghassemi, M.R., Shahpasandzadeh, M., Guest, B., Ashtiani, M.E., Yassaghi, A., and Kouhpeyma, M., 2013, History of faulting on the Doruneh fault system: Implications for the kinematic changes of the Central Iranian microplate: Geological Magazine, v. 150, no. 4, p. 651–672, doi:10.1017/S0016756812000751.

Khadivi, S., Mouthereau, F., Barbarand, J., Adatte, T., and Lacombe, O., 2012, Constraints on palaeodrainage evolution induced by uplift and exhumation on the southern flank of the Zagros–Iranian Plateau: Journal of the Geological Society of London, v. 169, no. 1, p. 83–97, doi:10.1144/0016-76492011-031.

Khadivi, S., Mouthereau, F., Larrasoaña, J.C., Vergés, J., Lacombe, O., Khademi, E., Beamud, E., Melinte-Dobrinescu, M., and Suc, J.P., 2010, Magnetochronology of synorogenic Miocene foreland sediments in the Fars arc of the Zagros folded belt (SW Iran): Basin Research, v. 22, no. 6, p. 918–932, doi:10.1111/j.1365-2117.2009.00446.x.

Le Guerroué, E., and Cobbold, P.R., 2006, Influence of erosion and sedimentation on strike-slip fault systems: Insights from analogue models: Journal of Structural Geology, v. 28, no. 3, p. 421–430, doi:10.1016/j.jsg.2005.11.007.

Madanipour, S., Ehlers, T.A., Yassaghi, A., Rezaeian, M., Enkelmann, E., and Bahroudi, A., 2013, Synchronous deformation on orogenic plateau margins: Insights from the Arabia-Eurasia collision: Tectonophysics, v. 608, p. 440–451, doi:10.1016/j.tecto.2013.09.003.

Matenco, L., Bertotti, G., Leever, K., Cloetingh, S., Schmid, S.M., Tărăpoancă, M., and Dinu, C., 2007, Large-scale deformation in a locked collisional boundary: Interplay between subsidence and uplift, intraplate stress, and inherited lithospheric structure in the late stage of the SE Carpathians evolution: Tectonics, v. 26, no. 4, TC4011, doi:10.1029/2006TC001951.

Mattei, M., Cifelli, F., Muttoni, G., Zanchi, A., Berra, F., Mossavvari, F., and Eshraghi, S.A., 2012, Neogene block rotation in central Iran: Evidence from paleomagnetic data: Geological Society of America Bulletin, v. 124, no. 5–6, p. 943–956, doi:10.1130/B30479.1.

McClusky, S., Reilinger, R., Mahmoud, S., Ben Sari, D., and Tealeb, A., 2003, GPS constraints on Africa (Nubia) and Arabia plate motions: Geophysical Journal International, v. 155, no. 1, p. 126–138, doi:10.1046/j.1365-246X.2003.02023.x.

McQuarrie, N., and van Hinsbergen, D.J.J., 2013, Retrodeforming the Arabia-Eurasia collision zone: Age of collision versus magnitude of continental subduction: Geology, v. 41, no. 3, p. 315–318, doi:10.1130/g33591.1.

McQuarrie, N., Stock, J.M., Verdel, C., and Wernicke, B.P., 2003, Cenozoic evolution of Neotethys and implications for the causes of plate motions: Geophysical Research Letters, v. 30, no. 20, p. 2036, doi:10.1029/2003GL017992.

Meyer, B., and Le Dortz, K., 2007, Strike-slip kinematics in central and eastern Iran: Estimating fault slip-rates averaged over the Holocene: Tectonics, v. 26, no. 5, TC5009, doi:10.1029/2006TC002073.

Meyer, B., Mouthereau, F., Lacombe, O., and Agard, P., 2006, Evidence of Quaternary activity along the Deshir fault: Implication for the Tertiary tectonics of central Iran: Geophysical Journal International, v. 164, no. 1, p. 192–201, doi:10.1111/j.1365-246X.2005.02784.x.

Molnar, P., 1988, Continental tectonics in the aftermath of plate tectonics: Nature, v. 335, no. 6186, p. 131–137, doi:10.1038/335131a0.

Molnar, P., and Tapponnier, P., 1975, Cenozoic tectonics of Asia: Effects of a continental collision: Science, v. 189, no. 4201, p. 419–426, doi:10.1126/science.189.4201.419.

Molnar, P., Anderson, R.S., and Anderson, S.P., 2007, Tectonics, fracturing of rock, and erosion: Journal of Geo-

physical Research–Earth Surface, v. 112, F03014, doi:10.1029/2005jf000433.

Morley, C.K., 2007, Variations in late Cenozoic–Recent strike-slip and oblique-extensional geometries, within Indochina: The influence of pre-existing fabrics: Journal of Structural Geology, v. 29, no. 1, p. 36–58, doi:10.1016/j.jsg.2006.07.003.

Morley, C.K., Kongwung, B., Julapour, A.A., Abdolghafourian, M., Hajian, M., Waples, D., Warren, J., Otterdoom, H., Srisuriyon, K., and Kazemi, H., 2009, Structural development of a major late Cenozoic basin and transpressional belt in central Iran: The Central Basin in the Qom-Saveh area: Geosphere, v. 5, no. 4, p. 325–362, doi:10.1130/GES00223.1.

Mouthereau, F., 2011, Timing of uplift in the Zagros belt/Iranian Plateau and accommodation of late Cenozoic Arabia-Eurasia convergence: Geological Magazine, v. 148, no. 5–6, p. 726–738, doi:10.1017/S0016756811000306.

Mouthereau, F., Tensi, J., Bellahsen, N., Lacombe, O., De Boisgrollier, T., and Kargar, S., 2007, Tertiary sequence of deformation in a thin-skinned/thick-skinned collision belt: The Zagros folded belt (Fars, Iran): Tectonics, v. 26, no. 5, TC5006, doi:10.1029/2007TC002098.

Mouthereau, F., Lacombe, O., and Vergés, J., 2012, Building the Zagros collisional orogen: Timing, strain distribution and the dynamics of Arabia/Eurasia plate convergence: Tectonophysics, v. 532–535, p. 27–60, doi:10.1016/j.tecto.2012.01.022.

Nozaem, R., Mohajjel, M., Rossetti, F., Della Seta, M., Vignaroli, G., Yassaghi, A., Salvini, F., and Eliassi, M., 2013, Post-Neogene right-lateral strike-slip tectonics at the north-western edge of the Lut block (Kuh-e-Sarhangi fault), central Iran: Tectonophysics, v. 589, p. 220–233, doi:10.1016/j.tecto.2013.01.001.

Okay, A.I., Zattin, M., and Cavazza, W., 2010, Apatite fission-track data for the Miocene Arabia-Eurasia collision: Geology, v. 38, no. 1, p. 35–38, doi:10.1130/G30234.1.

Paterson, M.S., and Wong, T.-F., 2005, Experimental Rock Deformation—The Brittle Field: New York, Springer Science & Business Media, 348 p.

Pavlis, T.L., Enkelmann, E., Gulick, S.P.S., and Pavlis, G.L., 2014, Introduction: Neogene tectonics and climate-tectonic interactions in the southern Alaskan orogen themed issue: Geosphere, v. 10, no. 3, p. 424–427, doi:10.1130/GES01023.1.

Petit, J.P., 1987, Criteria for the sense of movement on fault surfaces in brittle rocks: Journal of Structural Geology, v. 9, no. 5–6, p. 597–608, doi:10.1016/0191-8141(87)90145-3.

Raimondo, T., Hand, M., and Collins, W.J., 2014, Compressional intracontinental orogens: Ancient and modern perspectives: Earth-Science Reviews, v. 130, p. 128–153, doi:10.1016/j.earscirev.2013.11.009.

Ramezani, J., and Tucker, R.D., 2003, The Saghand region, central Iran: U-Pb geochronology, petrogenesis and implications for Gondwana tectonics: American Journal of Science, v. 303, no. 7, p. 622–665, doi:10.2475/ajs.303.7.622.

Reading, H.G., 2009, Sedimentary Environments: Processes, Facies and Stratigraphy: Oxford, John Wiley & Sons, 704 p.

Reece, R.S., Gulick, S.P.S., Christeson, G.L., Horton, B.K., van Avendonk, H., and Barth, G., 2013, The role of farfield tectonic stress in oceanic intraplate deformation, Gulf of Alaska: Journal of Geophysical Research–Solid Earth, v. 118, no. 5, p. 1862–1872, doi:10.1002/jgrb.50177.

Regard, V., Bellier, O., Thomas, J.-C., Bourlès, D., Bonnet, S., Abbassi, M.R., Braucher, R., Mercier, J., Shabanian, E., Soleymani, S., and Feghhi, K., 2005, Cumulative right-lateral fault slip rate across the Zagros-Makran transfer zone: Role of the Minab-Zendan fault system in accommodating Arabia-Eurasia convergence in southeast Iran: Geophysical Journal International, v. 162, no. 1, p. 177–203, doi:10.1111/j.1365-246X.2005.02558.x.

Regard, V., Bellier, O., Braucher, R., Gasse, F., Bourlès, D., Mercier, J., Thomas, J.C., Abbassi, M.R., Shabanian, E., and Soleymani, S., 2006, $^{10}$Be dating of alluvial deposits from southeastern Iran (the Hormoz Strait area): Palaeogeography, Palaeoclimatology, Palaeoecology, v. 242, no. 1–2, p. 36–53, doi:10.1016/j.palaeo.2006.05.012.

Regard, V., Hatzfeld, D., Molinaro, M., Aubourg, C., Bayer, R., Bellier, O., Yamini-Fard, F., Peyret, M., and Abbassi, M., 2010, The transition between Makran subduction and the Zagros collision: Recent advances in its structure and active deformation, *in* Leturmy, P., and Robin, C., eds., Tectonic and Stratigraphic Evolution of Zagros and Makran during the Mesozoic–Cenozoic: Geological Society of London Special Publication 330, p. 43–64, doi:10.1144/SP330.4.

Reilinger, R., McClusky, S., Vernant, P., Lawrence, S., Ergintav, S., Cakmak, R., Ozener, H., Kadirov, F., Guliev, I., Stepanyan, R., Nadariya, M., Hahubia, G., Mahmoud, S., Sakr, K., ArRajehi, A., Paradissis, D., Al-Aydrus, A., Prilepin, M., Guseva, T., Evren, E., Dmitrotsa, A., Filikov, S. V., Gomez, F., Al-Ghazzi, R., and Karam, G., 2006, GPS constraints on continental deformation in the Africa-Arabia-Eurasia continental collision zone and implications for the dynamics of plate interactions: Journal of Geophysical Research–Solid Earth, v. 111, B05411, doi:10.1029/2005jb004051.

Rezaeian, M., Carter, A., Hovius, N., and Allen, M.B., 2012, Cenozoic exhumation history of the Alborz Mountains, Iran: New constraints from low-temperature chronometry: Tectonics, v. 31, no. 2, TC2004, doi:10.1029/2011TC002974.

Robert, A M M., Letouzey, J., Kavoosi, M.A., Sherkati, S., Müller, C., Vergés, J., and Aghababaei, A., 2014, Structural evolution of the Kopeh Dagh fold-and-thrust belt (NE Iran) and interactions with the South Caspian Sea Basin and Amu Darya Basin: Marine and Petroleum Geology, v. 57, p. 68–87, doi:10.1016/j.marpetgeo.2014.05.002.

Robertson, A.H.F., Ustaömer, T., Parlak, O., Ünlügenç, U.C., Taşlı, K., and İnan, N., 2006, The Berit transect of the Tauride thrust belt, S Turkey: Late Cretaceous–early Cenozoic accretionary/collisional processes related to closure of the southern Neotethys: Journal of Asian Earth Sciences, v. 27, no. 1, p. 108–145, doi:10.1016/j.jseaes.2005.02.004.

Ron, H., Freund, R., Garfunkel, Z., and Nur, A., 1984, Block rotation by strike-slip faulting: Structural and paleomagnetic evidence: Journal of Geophysical Research–Solid Earth, v. 89, p. 6256–6270, doi:10.1029/JB089iB07p06256.

Rossetti, F., Lisker, F., Storti, F., and Läufer, A.L., 2003, Tectonic and denudational history of the Rennick graben (North Victoria Land): Implications for the evolution of rifting between East and West Antarctica: Tectonics, v. 22, no. 2, p. 1016, doi:10.1029/2002TC001416.

Rossetti, F., Nozaem, R., Lucci, F., Vignaroli, G., Gerdes, A., Nasrabadi, M., and Theye, T., 2015, Tectonic setting and geochronology of the Cadomian (Ediacaran–Cambrian) magmatism in central Iran, Kuh-e-Sarhangi region (NW Lut block): Journal of Asian Earth Sciences, v. 102, p. 24–44, doi:10.1016/j.jseaes.2014.07.034.

Rowland, J.V., and Sibson, R.H., 2004, Structural controls on hydrothermal flow in a segmented rift system, Taupo volcanic zone, New Zealand: Geofluids, v. 4, no. 4, p. 259–283, doi:10.1111/j.1468-8123.2004.00091.x.

Rutter, E.H., and Hadizadeh, J., 1991, On the influence of porosity on the low-temperature brittle-ductile transition in siliciclastic rocks: Journal of Structural Geology, v. 13, no. 5, p. 609–614, doi:10.1016/0191-8141(91)90047-M.

Salvini, F., 2004, Daisy 3: The Structural Data Integrated System Analyzer Software: University of Roma Tre, Roma: http://host.uniroma3.it/progetti/fralab (accessed 7 July 2015).

Salvini, F., Brancolini, G., Busetti, M., Storti, F., Mazzarini, F., and Coren, F., 1997, Cenozoic geodynamics of the Ross Sea region, Antarctica: Crustal extension, intraplate strike-slip faulting, and tectonic inheritance: Journal of Geophysical Research–Solid Earth, v. 102, p. 24,669–24,696, doi:10.1029/97JB01643.

Sanderson, D.J., and Marchini, W.R.D., 1984, Transpression: Journal of Structural Geology, v. 6, no. 5, p. 449–458, doi:10.1016/0191-8141(84)90058-0.

Sandiford, M., Wallace, M., and Coblentz, D., 2004, Origin of the in situ stress field in south-eastern Australia: Basin Research, v. 16, no. 3, p. 325–338, doi:10.1111/j.1365-2117.2004.00235.x.

Scholz, C.H., 2002, The Mechanics of Earthquakes and Faulting: Cambridge, UK, Cambridge University Press, 504 p.

Schopfer, M.P., and Steyrer, H.P., 2001, Experimental modeling of strike-slip faults and the self-similar behavior, *in* Koyi, H.A., and Mancktelow, N.S., eds., Tectonic Modeling: A Volume in Honor of Hans Ramberg: Geological Society of America Memoir 193, p. 21–28.

Schrank, C.E., and Cruden, A.R., 2010, Compaction control of topography and fault network structure along strike-slip faults in sedimentary basins: Journal of Structural Geology, v. 32, no. 2, p. 184–191, doi:10.1016/j.jsg.2009.11.003.

Sella, G. F., Dixon, T. H., and Mao, A., 2002, Revel: A model for recent plate velocities from space geodesy: Journal of Geophysical Research, v. 107, p. 209–226, doi:10.1029/2000JB000033.

Shabanian, E., Bellier, O., Siame, L., Arnaud, N., Abbassi, M.R., and Cochemé, J.-J., 2009a, New tectonic configuration in NE Iran: Active strike-slip faulting between the Kopeh Dagh and Binalud Mountains: Tectonics, v. 28, no. 5, TC5002, doi:10.1029/2008TC002444.

Shabanian, E., Siame, L., Bellier, O., Benedetti, L., and Abbassi, M.R., 2009b, Quaternary slip rates along the northeastern boundary of the Arabia-Eurasia collision zone (Kopeh Dagh Mountains, northeast Iran): Geophysical Journal International, v. 178, no. 2, p. 1055–1077, doi:10.1111/j.1365-246X.2009.04183.x.

Shabanian, E., Bellier, O., Abbassi, M.R., Siame, L., and Farbod, Y., 2010, Plio-Quaternary stress states in NE Iran: Kopeh Dagh and Allah Dagh-Binalud mountain ranges: Tectonophysics, v. 480, no. 1–4, p. 280–304, doi:10.1016/j.tecto.2009.10.022.

Sheldon, H.A., Barnicoat, A.C., and Ord, A., 2006, Numerical modelling of faulting and fluid flow in porous rocks: An approach based on critical state soil mechanics: Journal of Structural Geology, v. 28, no. 8, p. 1468–1482, doi:10.1016/j.jsg.2006.03.039.

Simons, W.J.F., Socquet, A., Vigny, C., Ambrosius, B.A.C., Haji Abu, S., Promthong, C., Subarya, C., Sarsito, D.A., Matheussen, S., Morgan, P., and Spakman, W., 2007, A decade of GPS in Southeast Asia: Resolving Sundaland motion and boundaries: Journal of Geophysical Research–Solid Earth, v. 112, B06420, doi:10.1029/2005jb003868.

Spotila, J.A., Farley, K.A., and Sieh, K., 1998, Uplift and erosion of the San Bernardino Mountains associated with transpression along the San Andreas fault, California, as constrained by radiogenic helium thermochronometry: Tectonics, v. 17, no. 3, p. 360–378, doi:10.1029/98TC00378.

Spotila, J.A., Farley, K.A., Yule, J.D., and Reiners, P.W., 2001, Near-field transpressive deformation along the San Andreas fault zone in southern California, based on exhumation constrained by (U-Th)/He dating: Journal of Geophysical Research–Solid Earth, v. 106, p. 30,909–30,922, doi:10.1029/2001JB000348.

Spotila, J.A., Niemi, N., Brady, R., House, M., Buscher, J., and Oskin, M., 2007, Long-term continental deformation associated with transpressive plate motion: The San Andreas fault: Geology, v. 35, no. 11, p. 967–970, doi:10.1130/g23816a.1.

Storti, F., Holdsworth, R.E., and Salvini, F., 2003, Intraplate strike-slip deformation belts, *in* Storti, F., Holdsworth, R.E., and Salvini, F., eds., Intraplate Strike-Slip Deformation Belts: Geological Society of London Special Publication 210, p. 1–14, doi:10.1144/GSL.SP.2003.210.01.01.

Sutton, J., and Watson, J.V., 1986, Architecture of the continental lithosphere: Philosophical Transactions of the Royal Society of London, ser. A: Mathematical, Physical and Engineering Sciences, v. 317, no. 1539, p. 5–12, doi:10.1098/rsta.1986.0020.

Sylvester, A.G., 1988, Strike-slip faults: Geological Society of America Bulletin, v. 100, no. 11, p. 1666–1703, doi:10.1130/0016-7606(1988)100<1666:SSF>2.3.CO;2.

Tapponnier, P., and Molnar, P., 1977, Active faulting and tectonics in China: Journal of Geophysical Research, v. 82, p. 2905–2930, doi:10.1029/JB082i020p02905.

Tavarnelli, E., 1998, Tectonic evolution of the northern Salinian block, California, USA: Paleogene to Recent shortening in a transform fault-bounded continental fragment, *in* Holdsworth, R.E., Strachan, R.A., and Dewey, J.E., eds., Continental Transpressional and Transtensional Tectonics: Geological Society of London Special Publication 135, p. 107–118.

Tavarnelli, E., and Holdsworth, R.E., 1999, How long do structures take to form in transpression zones? A cautionary tale from California: Geology, v. 27, no. 12, p. 1063–1066, doi:10.1130/0091-7613(1999)027<1063:HLDSTT>2.3.CO;2.

Tavarnelli, E., and Pasqui, V., 2000, Fault growth by segment linkage in seismically active settings: Examples from the Southern Apennines, Italy, and the Coast Ranges, California: Journal of Geodynamics, v. 29, p. 501–516, doi:10.1016/S0264-3707(99)00041-1.

Tchalenko, J.S., Berberian, M., and Behzadi, H., 1973, Geomorphic and seismic evidence for recent activity on the Doruneh fault, Iran: Tectonophysics, v. 19, no. 4, p. 333–341, doi:10.1016/0040-1951(73)90027-9.

Verdel, C., Wernicke, B.P., Ramezani, J., Hassanzadeh, J., Renne, P.R., and Spell, T.L., 2007, Geology and thermochronology of Tertiary Cordilleran-style metamorphic core complexes in the Saghand region of central Iran: Geological Society of America Bulletin, v. 119, no. 7–8, p. 961–977, doi:10.1130/B26102.1.

Vernant, P., Nilforoushan, F., Hatzfeld, D., Abbassi, M.R., Vigny, C., Masson, F., Nankali, H., Martinod, J., Ashtiani, A., Bayer, R., Tavakoli, F., and Chéry, J., 2004, Present-day crustal deformation and plate kinematics in the Middle East constrained by GPS measurements in Iran and northern Oman: Geophysical Journal International, v. 157, no. 1, p. 381–398, doi:10.1111/j.1365-246X.2004.02222.x.

Vincent, S.J., Morton, A.C., Carter, A., Gibbs, S., and Barabadze, T.G., 2007, Oligocene uplift of the Western Greater Caucasus: An effect of initial Arabia-Eurasia collision: Terra Nova, v. 19, no. 2, p. 160–166, doi:10.1111/j.1365-3121.2007.00731.x.

Walker, R., and Jackson, J., 2004, Active tectonics and late Cenozoic strain distribution in central and eastern Iran: Tectonics, v. 23, no. 5, doi:10.1029/2003TC001529.

Walker, R., Jackson, J., and Baker, C., 2004, Active faulting and seismicity of the Dasht-e-Bayaz region, eastern Iran: Geophysical Journal International, v. 157, no. 1, p. 265–282, doi:10.1111/j.1365-2966.2004.02179.x.

Walker, R.T., and Fattahi, M., 2011, A framework of Holocene and late Pleistocene environmental change in eastern Iran inferred from the dating of periods of alluvial fan abandonment, river terracing, and lake deposition: Quaternary Science Reviews, v. 30, no. 9–10, p. 1256–1271, doi:10.1016/j.quascirev.2011.03.004.

Walker, R.T., and Khatib, M.M., 2006, Active faulting in the Birjand region of NE Iran: Tectonics, v. 25, no. 4, TC4016, doi:10.1029/2005TC001871.

Walpersdorf, A., Manighetti, I., Mousavi, Z., Tavakoli, F., Vergnolle, M., Jadidi, A., Hatzfeld, D., Aghamohammadi, A., Bigot, A., Djamour, Y., Nankali, H., and Sedighi, M., 2014, Present-day kinematics and fault slip rates in eastern Iran, derived from 11 years of GPS data: Journal of Geophysical Research–Solid Earth, v. 119, no. 2, p. 1359–1383, doi:10.1002/2013JB010620.

Webb, L.E., and Johnson, C.L., 2006, Tertiary strike-slip faulting in southeastern Mongolia and implications for Asian tectonics: Earth and Planetary Science Letters, v. 241, no. 1–2, p. 323–335, doi:10.1016/j.epsl.2005.10.033.

Wong, T.-f., and Baud, P., 2012, The brittle-ductile transition in porous rock: A review: Journal of Structural Geology, v. 44, p. 25–53, doi:10.1016/j.jsg.2012.07.010.

Woodcock, N.H., and Fischer, M., 1986, Strike-slip duplexes: Journal of Structural Geology, v. 8, no. 7, p. 725–735, doi:10.1016/0191-8141(86)90021-0.

Woodcock, N.H., and Rickards, B., 2003, Transpressive duplex and flower structure: Dent fault system, NW England: Journal of Structural Geology, v. 25, no. 12, p. 1981–1992, doi:10.1016/S0191-8141(03)00057-9.

Woodcock, N.H., and Schubert, C., 1994, Continental strike-slip tectonics, *in* Hancock, P.L., ed., Continental Deformation: Oxford, Pergamon Press, p. 251–263.

Wu, J. E., McClay, K., Whitehouse, P., and Dooley, T., 2009, 4D analogue modelling of transtensional pull-apart basins: Marine and Petroleum Geology, v. 26, no. 8, p. 1608–1623, doi:10.1016/j.marpetgeo.2008.06.007.

Ziegler, P.A., van Wees, J.-D., and Cloetingh, S., 1998, Mechanical controls on collision-related compressional intraplate deformation: Tectonophysics, v. 300, no. 1–4, p. 103–129, doi:10.1016/S0040-1951(98)00236-4.

Zoback, M.L., 1992, First- and second-order patterns of stress in the lithosphere: The World Stress Map Project: Journal of Geophysical Research–Solid Earth, v. 97, p. 11,703–11,728, doi:10.1029/92JB00132.